Lithos 288–289 (2017) 125–142

Contents lists available at ScienceDirect

Lithos

journal homepage: www.elsevier.com/locate/lithos

Petrogenesis of Cretaceous shoshonitic rocks in the northern Wuyi Mountains, South China: A result of the roll-back of a flat-slab?

Wu-Xian Li [a,*], Xian-Hua Li [b], Xuan-Ce Wang [c,d], Dong-Sheng Yang [e]

[a] State Key Laboratory of Isotopic Geochemistry, Guangzhou Institute of Geochemistry, Chinese Academy of Sciences, Guangzhou 510640, China
[b] State Key Laboratory of Lithospheric Evolution, Institute of Geology and Geophysics, Chinese Academy of Sciences, Beijing 100029, China
[c] The Institute for Geoscience Research (TIGeR), Department of Applied Geology, Curtin University, GPO Box U1987, Perth, WA 6845, Australia
[d] School of Earth Science and Resources, Chang'an University, Xi'an, Shanxi 710054, China
[e] Key Laboratory of Mineralogy and Metallogeny, Guangzhou Institute of Geochemistry, Chinese Academy of Sciences, Guangzhou 510640, China

ARTICLE INFO

Article history:
Received 6 February 2017
Accepted 14 June 2017
Available online 27 July 2017

Keywords:
Potassic magmatism
Shoshonitic rocks
Flat-slab delamination
Early Cretaceous
South China

ABSTRACT

Potassic magmatism is commonly linked to post-/late-orogenic environments, such as foundering or convection thinning of continental lithosphere. Their petrogenesis is crucial for constraining the chemical and physical properties of the remnant sub-continental lithospheric mantle. Here we report new SHRIMP zircon U–Pb ages, whole rock geochemical results and Sr–Nd and zircon Hf isotope data from four potassic plutons (the Da'an, Yingcheng, Zixi and Honggong plutons) in the northern Wuyi Mountains, South China. SHRIMP U–Pb zircon analyses indicate that these potassic rocks formed at 139–126 Ma. They are characterized by high SiO_2 (56–73%) and K_2O (3.8–6.7%), with a K_2O/Na_2O ratio of 2.18–2.04, plotting within the field of high-SiO_2 shoshonites. Their I_{Sr} and εNd(t) values vary from 0.7077 to 0.7162 and −5.66 to −10.52, respectively. The initial zircon εHf(t) values range from 2.3 to −13.1, corresponding to T_{DM} modal ages between 707 and 1330 Ma. These geochemical and isotope characteristics indicate that these shoshonites derived from a subduction-modified ancient subcontinental lithospheric mantle, and then underwent significantly fractional crystallization of K-feldspar, plagioclase, and accessory minerals, such as apatite and Fe–Ti oxides during magma ascent. We interpret that asthenospheric mantle upwelling (caused by eastward roll-back of a flat-slab?) triggered partial melting of the metasomatized lithospheric mantle to result in the Early Cretaceous shoshonitic magmatism in the northern Wuyi Mountains. An integration of our new results with compiled data from the interior of the South China Block reveals that the arc-like geochemical signature is confined to the Wuyi Mountains region, but becomes little or even invisible toward inland in South China. This implies that the far-field effects of the early Mesozoic subduction only reached the Wuyi Mountains, ca. 500 km away from the trench, consistent with flat or shallow subduction models.

1. Introduction

Petrogenesis of potassic rocks from the Sierra Nevada of California, USA (Manley et al., 2000), the westernmost Mediterranean (Duggen et al., 2003, 2005), and Tibetan plateau (Chung et al., 1998; Turner et al., 1993; Williams et al., 2004) shows that small-volume potassic magmatic rocks with arc signatures are often attributed to low-degree melting of the remnant sub-continental lithospheric mantle caused by hot asthenosphere upwelling as a result of foundering or convection removal of continental lithosphere (e.g., Chung et al., 1998; Duggen et al., 2003, 2005; Kay and Kay, 1993; Manley et al., 2000; Turner et al., 1993, 1996; Williams et al., 2004). Therefore, potassic and/or shoshonitic rocks are usually regarded as an important petrological index for the foundering and/or thinning of the lithospheric mantle (Manley et al., 2000).

Late Mesozoic igneous rocks are widespread in southeastern China and cover an exposed area of ca. 218,000 km^2 (Zhou et al., 2006) (Fig. 1a). They are dominantly Jurassic (~190–155 Ma, known as the "Early Yanshanian" event) and Cretaceous (145–80 Ma, known as the "Late Yanshanian" event) in age (e.g. Cen et al., 2016; Li, 2000; Li et al., 2007; Zhou and Li, 2000; Zhou et al., 2006). The Jurassic igneous rocks are mainly distributed in the continental interior, consisting predominantly of bimodal volcanic/intrusive rocks (~190 Ma), as well as large granitic batholiths (165–155 Ma). The Cretaceous igneous rocks occur dominantly in the coast areas, east of the Wuyi Mountains, and are composed predominantly of felsic volcanic and intrusive rocks (>95%) plus minor mafic rocks. In addition, minor amounts of shoshonitic to ultra-potassic rocks are sporadically distributed from the interior of South China to the Wuyi Mountains region (Fig. 1a). These ultra-potassic to shoshonitic rocks were interpreted to be formed by partial melting of an enriched sub-lithospheric mantle owing to a raised geotherm caused by lithosphere thinning (Li et al., 2004a). However, the ages and petrogenesis of shoshonitic rocks in the northern Wuyi

* Corresponding author.
E-mail address: liwx@gig.ac.cn (W.-X. Li).

http://dx.doi.org/10.1016/j.lithos.2017.06.014
0024-4937/

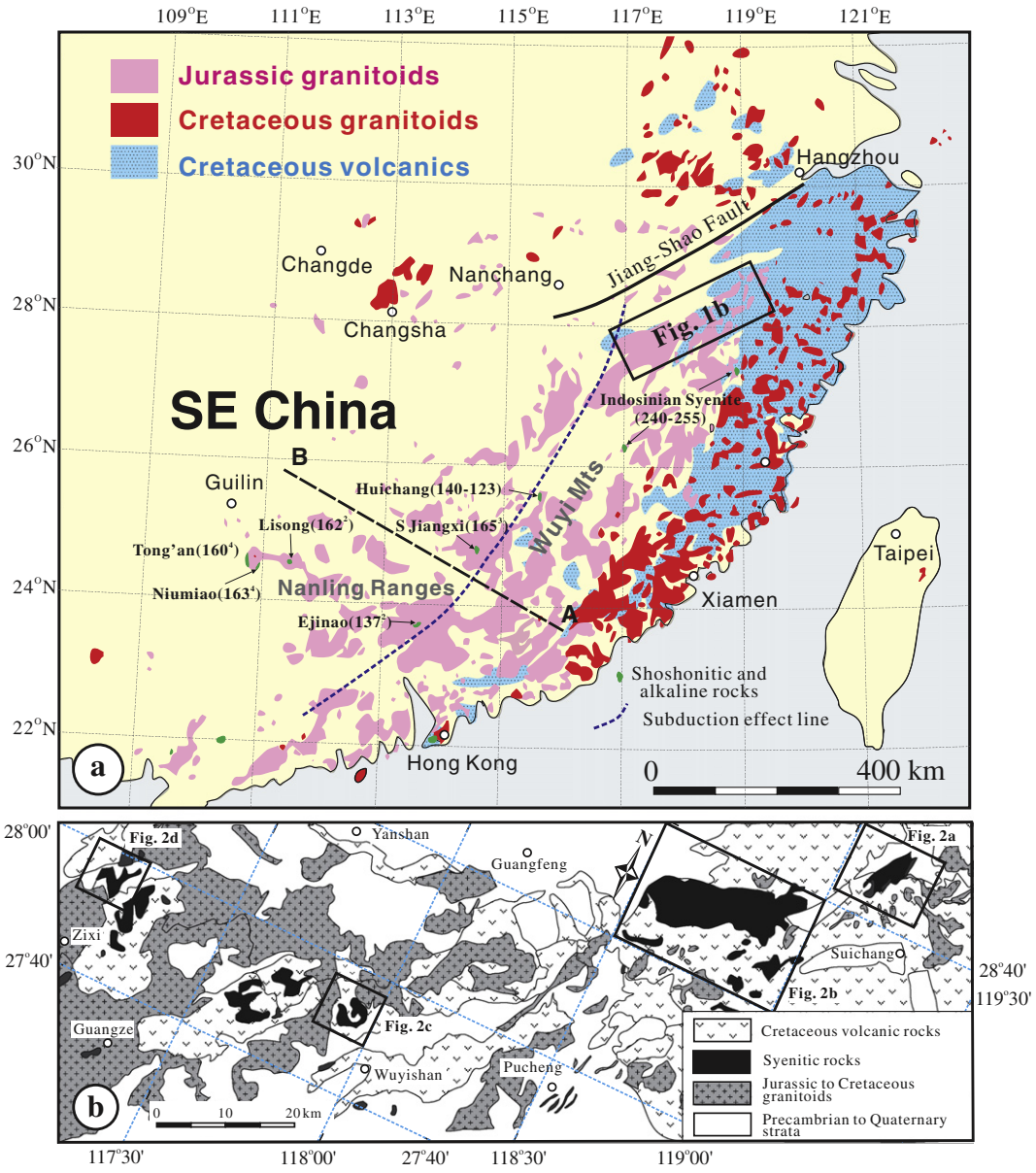

Fig. 1. (a) A simplified map showing the distribution of Late Mesozoic igneous rocks in Southeast China (modified after Li et al., 2007), and (b) locations of the shoshonitic plutons in the northern Wuyi Mountains region.

Mountains are still poorly constrained. In this paper, we report new SHRIMP U–Pb zircon age, zircon Hf isotope and whole rock geochemical results for these shoshonitic rocks, with the goal of investigating their origin and petro-tectonic implications.

2. Geological background

The South China Block consists of the Yangtze Block in the northwest and the Cathaysia Block in the southeast. The Jiangshan–Shaoxing Fault is conventionally regarded as the eastern boundary separating the two blocks. The Yangtze Block consists of dominant greenschist-facies metamorphic early Neoproterozoic arc volcanic rocks and rift-related sedimentary sequences (Li et al., 2008, 2009, 2010; Ye et al., 2007), whereas the Cathaysia Block mainly composes of high-grade metamorphic Paleoproterozoic to Neoproterozoic volcanic–sedimentary rocks (Li, 1997; Li et al., 2010; Yu et al., 2009). There are several small potassic plutons with hypabyssal to subvolcanic facies outcropped along the northern margin of the Wuyi Mountain region in the Cathaysia Block (Fig. 1a, b). For the exception of the Honggong pluton which has an outcrop area of over 450 km^2, the potassic intrusions are typically <100 km^2 each. In this paper, four potassic plutons were selected for detailed geochronology, geochemistry, and whole rock Sr–Nd and zircon Hf isotopic studies. They are, from east to west, the Yingcheng, Honggong, Da'an and Zixi plutons.

The Yingcheng pluton has an area of ~60 km^2 and is an amphibole–biotite-bearing quartz monzonite (Fig. 2a). Some dark elliptical enclaves, mostly between 10 and 15 cm in diameter, were observed occasionally in the quartz monzonite (Lu et al., 2006a). The quartz monzonite consists of about 35–40% K-feldspar, 40–45% plagioclase (An = 30–35), 5–8% quartz, 5–15% amphibole and biotite, as well as accessory minerals including zircon, apatite and Fe–Ti oxides. Most of the mafic minerals, i.e. biotite and amphibole, have been altered to chlorite. The mafic enclaves are monzodiorite, and have the same mineral assemblage as the quartz monzonite but have a higher percentage of mafic mineral. The pluton intrudes Precambrian metamorphic rocks, and faulted contact with Cretaceous volcanic rocks. A 141 ± 7 Ma whole rock Rb–Sr isochrone age is reported for this pluton (Lu et al., 2006a).

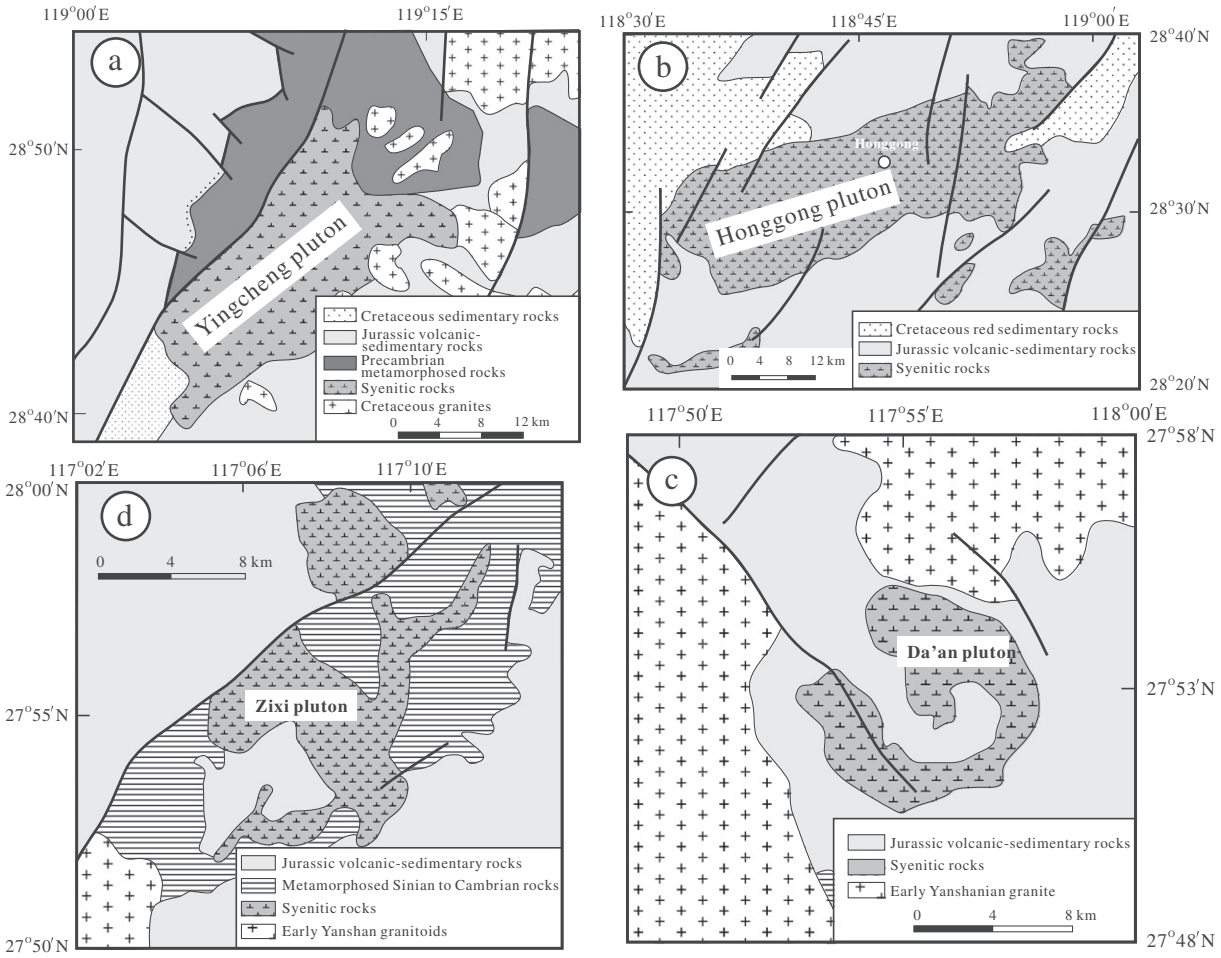

Fig. 2. Geological maps of (a) the Yingcheng pluton, (b) the Honggong pluton, (c) the Da'an pluton, and (d) the Zixi pluton. Locations of these plutons are shown in Fig. 1.

The Honggong pluton is the largest one in the northern Wuyi Mountains with NEE-trends (Fig. 2b). It intrudes early Cretaceous volcanic rocks and is covered by late Cretaceous sedimentary rocks. The main rock-type of the pluton is biotite–hornblende-bearing syenite and quartz-monzonite. The rocks are commonly dark gray to pink in color owing to the abundance of K-feldspar. The mineral assemblage consists of 55–65% K-feldspar (mainly microcline), 6–20% quartz, 8–20% plagioclase (An = 25–30), 5–15% amphibole and biotite, plus accessory minerals zircon, apatite and Fe–Ti oxides. Zircon is also found to aggregate around the Fe–Ti oxides in thin sections. The pluton was previously considered either a I-type granite due to the presence of amphibole (Chen et al., 1991), or an A-type granite due to its high abundance in incompatible elements (Lu et al., 2006b). Chen et al. (1991) reported a hornblende Ar–Ar age of 124 ± 1 Ma for the pluton, and a most recent La-ICP-MS zircon U–Pb dating gave an age of 127.2 ± 1.6 Ma (He and Xu, 2012).

The Da'an pluton is a ring-shaped subvolcanic intrusion with an outcrop area of ~80 km^2 (Fig. 2c). It is comprised of quartz monzonite with minor syenite, consisting of 40–50% K-feldspar, 40–50% plagioclase, 5–10% quartz, and accessory minerals zircon, apatite and Fe–Ti oxides (mainly magnetite). Most of the K-feldspar and plagioclase are strongly altered, leading to argillization and sericitization, respectively. The rocks display a granophyric texture, suggesting a shallow level emplacement.

The Zixi pluton has an outcrop area of ~90 km^2, and intrudes metamorphosed Sinian to Cambrian strata and non-metamorphosed Jurassic volcanic–sedimentary sequences (Fig. 2d). It is predominantly a quartz syenite, consisting of K-feldspar (55–60%), plagioclase (30–35%), quartz (10–15%), and accessory minerals of zircon, apatite and Fe–Ti oxides. The quartz syenites display a granophyric structure, implying that the pluton was emplaced at a shallow level. Strong sericitization and argillization were observed in K-feldspar and plagioclase, respectively.

3. Analytical methods

Zircon grains were separated using standard density and magnetic separation techniques. Representative zircon grains were hand-picked under a binocular microscope. Zircon grains, together with zircon standard Temora, were cast in an epoxy mount, which was then polished to section the crystals in half for analysis. Zircons were documented with transmitted and reflected light micrographs as well as cathodoluminescence (CL) images to reveal their internal structures. Measurements of U, Th, and Pb were conducted using the SHRIMP II ion microprobe at the Beijing SHRIMP Center under standard operating conditions (5-scan cycle, 2 nA primary O_2^- beam, mass resolution ca. 5000). U–Th–Pb rations were determined relative to the TEMORA standard zircon with $^{206}Pb/^{238}U = 0.0668$ corresponding to 417 Ma (Black et al., 2003), and the absolute abundances were calibrated to the standard zircon SL13. Analyses of the TEMORA standard zircon were interspersed with those of unknowns, following operating and data processing procedures similar to those described by Williams (1998). Measured compositions were corrected for common Pb using the ^{204}Pb-method, and an average crustal composition (Cumming and Richards, 1975) appropriate to the age of the mineral was assumed. Uncertainties on individual analyses are reported at 1σ level, and mean ages for pooled $^{206}Pb/^{238}U$ results are quoted at 95% confidence level.

In situ zircon Lu–Hf isotopic analysis was carried out using a Neptune multi-collector ICP-MS equipped with a Geolas-193 laser-ablation system at the Institute of Geology and Geophysics. Most of

Lu–Hf isotopic analyses were obtained on the same zircons which were previously analyzed for U–Pb dating, with ablation pots of 63 μm in diameter, typical ablation time of 26 s, repetition rate of 10 Hz, and laser beam energy density of 15 mJ/cm^2. The detailed analytical procedures and instrumental setting were similar to those described by Wu et al. (2006). In order to evaluate the reliability of the analytical data, standard zircon 91500 and TEMORA were analyzed during the course of this study. Measured $^{176}Hf/^{177}Hf$ ratios were normalized to $^{179}Hf/^{177}Hf = 0.7325$, using exponential correction for mass bias. Further external adjustment is not applied for the unknowns because our determined $^{176}Hf/^{177}Hf$ ratios for zircon standards 91500 (0.282303 ± 0.000010) and TEMORA (0.282676 ± 0.00001) are in good agreement with the reported values (Griffin et al., 2006; Wu et al., 2006).

Major element oxides and trace elements were determined by using a Varian Vista PRO ICP-AES and a Perkin-Elmer Sciex ELAN 6000 ICP-MS, respectively, at the State Key Laboratory of Isotope Geochemistry, Guangzhou Institute of Geochemistry, Chinese Academy of Sciences (SKLaBIG, GIGCAS). Procedures for major element and trace element analyses were similar to those described by Li et al. (2002). About 40 mg powdered samples were dissolved in a platinum crucible using $Li_2B_4O_7 + H_3BO_3$ mixture at ca. 1100 °C for 20 min. For ICP-AES major element analysis, the sample dissolution was spiked with single element In as an internal standard for monitoring the signal drift during measurement, and diluted to a factor of 1/5000. A set of USGS and Chinese national rock standards was chosen for calibrating major element concentrations of unknowns. For ICP-MS trace element analysis, an internal standard solution containing the single element Rh was used with a dilution factor of 1/5000. The USGS standards W-2 and MRG-1 and the Chinese national rock standard GSR-1 were chosen for calibrating element concentrations of measured samples. Analytical precision is generally better than 5% for major elements by ICP-AES, and better than 10% for most trace elements by ICP-MS.

Sr and REE were separated using cation columns, and Nd fractions were further separated by HDEHP-coated Kef columns. Sr and Nd isotopic analyses were performed on a Micromass Isoprobe multi-collector ICPMS (MC-ICPMS) at the SKLaBIG, GIGCAS. Samples were taken up in 2% HNO_3, and the aqueous solutions were introduced into the MC-ICPMS using a Meinhard glass nebulizer with an uptake rate of 0.1 mL/min. The inlet system was washed out for 5 min between analyses using high-purity 5% HNO_3 followed by a blank solution of 2% HNO_3 from which the sample solutions were prepared. The Isoprobe MC-ICPMS was operated in a static mode, and yielded $^{143}Nd/^{144}Nd = 0.512125 \pm 11$ (2σ) on 14 runs for the Shin Etsu JNdi-1 standard during this study. Analytical procedures were similar to those described by Wei et al. (2002) and Li et al. (2004b). Measured $^{87}Sr/^{86}Sr$ and $^{143}Nd/^{144}Nd$ ratios were normalized to $^{86}Sr/^{88}Sr = 0.1194$ and $^{146}Nd/^{144}Nd = 0.7219$, respectively. The reported $^{87}Sr/^{86}Sr$ and $^{143}Nd/^{144}Nd$ ratios were respectively adjusted to the NBS SRM 987 Standard $^{87}Sr/^{86}Sr = 0.71025$ and the Shin Etsu JNdi-1 standard $^{143}Nd/^{144}Nd = 0.512115$ (Tanaka et al., 2000).

4. Results

4.1. SHRIMP U–Pb zircon geochronology

Sample Y-1-1 (28°45′06″; 119°12′53″) is collected from the Yingcheng quartz syenite. Zircon crystals from this sample are mostly euhedral, ranging from 100 to 250 μm in length with length to width ratios of about 2:1. They are generally transparent and colorless, showing typically magmatic internal zonation in CL images (Fig. 3a, inset). Fourteen analytical spots were conducted on 14 zircon grains. Uranium and thorium concentrations of these grains are in the ranges of 99 to 582 ppm and 119 to 352 ppm, respectively, and Th/U ratios vary from 0.59 to 1.53. The proportion of common ^{206}Pb in total measured ^{206}Pb (f_{206} in Appendix Table 1) varies between 0.86% and 6.86%, mostly clustering at 2–4%. The measured $^{206}Pb/^{238}U$ ratios are in good agreement

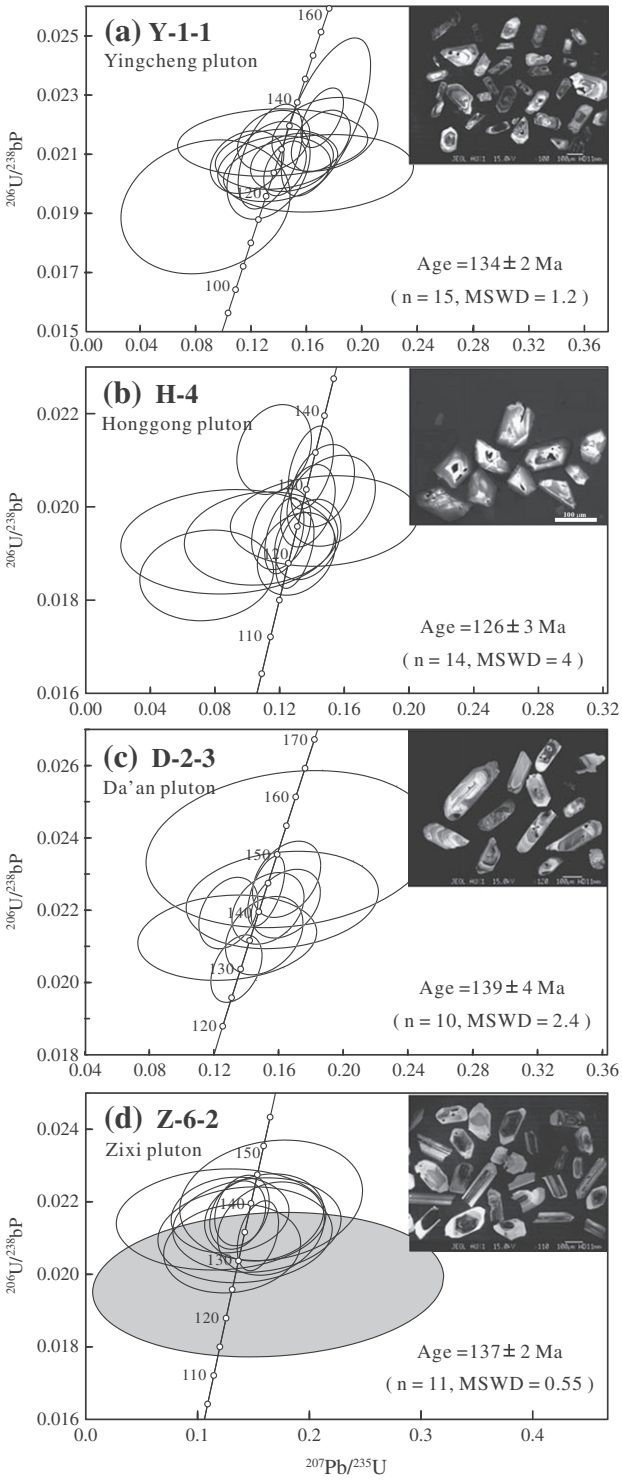

Fig. 3. SHRIMP zircon U–Pb Concordia diagrams for the shoshonitic rocks in the northern Wuyi Mountains region. (a) The Yingcheng syenite (Y-1-1); (b) the Da'an syenite (D-2-3); (c) the Zixi syenite (Z-6-2) and (d) the Honggong syenite (H-4). The insets show representative zircon CL images.

within analytical errors, corresponding to a single age population with a weighted mean $^{206}Pb/^{238}U$ age of 134 ± 2 Ma (95% confidence interval) (Fig. 3a). The age is considered as the best estimate of the crystallization age of the Yingcheng quartz syenite.

Sample H-4 (28°34′47″; 118°45′24″) is from the Honggong amphibole-bearing syenite. Zircon grains from the sample are relatively uniform in size (~100 μm) and mostly euhedral, with length to width

ratios between 1:1 and 2:1. They are generally transparent and colorless, and show magmatic internal zonation in CL images (Fig. 3b, inset). Fourteen analyses were conducted on 14 zircon grains. Uranium and thorium concentrations of these grains are in the ranges of 126–810 ppm and 123–1054 ppm, respectively. Th/U ratios range from 0.73 to 1.23. The proportion of common ^{206}Pb in measured ^{206}Pb (f_{206} in Appendix Table 1) is between 0 and 3.08%. The 14 analyses form a concordant population that yielded a weighted mean $^{206}Pb/^{238}U$ age of 125.7 ± 2.7 Ma (95% confidence interval). This age is interpreted as the formation age of the Honggong syenite, which coincides with the previously reported amphibole Ar–Ar age of 124 ± 1 Ma (Chen et al., 1991) and La-ICP-MS zircon U–Pb age of 127.2 ± 1.6 Ma (He and Xu, 2012).

Sample D-2-3 (27°52′01″; 117°54′09″) is from the Da'an quartz monzonite. Zircon gains from this sample are euhedral and show magmatic internal zonation in CL images (Fig. 3c, inset). They are 100–200 μm in length, with length to width ratios between 2:1 and 4:1. The majority of zircons are relatively transparent and colorless, although a few zircons are dark brown in color due to high uranium content. No inherited zircon core was observed in the CL images. Eleven analyses of 11 zircons were obtained. Thorium and uranium concentrations are in the range from 72 to 1525 ppm and 91 to 1005 ppm, respectively. Th/U ratios vary between 0.53 and 2.03, mostly clustering around 0.6–0.9. The proportion of common ^{206}Pb in total measured ^{206}Pb (f_{206} in Appendix Table 1) is between 0.46% and 3.91%, mainly clustering around 3%–4%. The measured $^{206}Pb/^{238}U$ ratios are in good agreement within analytical errors, yielding a weighted mean $^{206}Pb/^{238}U$ age of 139.3 ± 3.9 Ma (95% confidence interval) (Fig. 3c), interpreted as the crystallization age of the Da'an syenite.

Sample Z-6-2 (27°55′21″; 117°09′56″) is from the Zixi quartz syenite. Zircon grains are mostly euhedral. Crystal lengths are in the range of 100–300 μm, and length to width ratios are between 1:1 and 4:1. The zircon grains are mostly transparent and colorless, and have magmatic internal zonation in CL images (Fig. 3d, inset). Twelve analyses were conducted on 12 zircons. Uranium and thorium concentrations are in the range of 60–589 ppm and 44–562 ppm, respectively. Th/U ratios vary between 0.67 and 1.33. The proportion of common ^{206}Pb in total measured ^{206}Pb (f_{206} in Appendix Table 1) ranges between 0.42% and 7.36%, mainly clustering around 2%–4%. The measured $^{206}Pb/^{238}U$ ratios are in good agreement within analytical errors, with the exception of spot 7.1 which has a young age due to the significantly lower U (U = 44 ppm) and high common ^{206}Pb (f_{206} 7.36%) contents. The remaining 11 measurements yielded a weighted mean $^{206}Pb/^{238}U$ age of 136.6 ± 1.8 Ma (95% confidence interval) (Fig. 3d), which is interpreted as the crystallization age of the Zixi quartz syenite.

In summary, our SHRIMP U–Pb zircon dating results indicate that the studied potassic rocks in the northern Wuyi Mountains formed from ~140 Ma to ~125 Ma and belong to the Early Cretaceous (Late Yanshanian event).

4.2. Major and trace elements

Major and trace element data of thirty-seven samples are presented in Appendix Table 2. Among them, eight samples are from the Yingcheng pluton, fifteen from the Honggong pluton, eleven from the Da'an pluton, and three from the Zixi pluton.

The rocks have SiO_2 contents ranging from 60 to 73% and three enclave samples (YC-1-3, YC-1-4 and YC-1-5) have relatively lower SiO_2 content varying from 56% to 61%. As shown in the total alkalic vs. SiO_2 diagram (Fig. 4a), these rocks are mainly plotted within the fields of quartz-monzonite and syenite. Two enclave samples (YC-1-3 and YC-1-5) are plotted into the field of monzonite, and three highly-evolved samples (one from the Da'an and two from the Yingcheng plutons) are plotted into the granite field. Most of the samples are plotted within the field defined by the Tibetan Plateau Cenozoic shoshonitic rocks (Chung et al., 1998) (Fig. 4a). Although the samples were collected

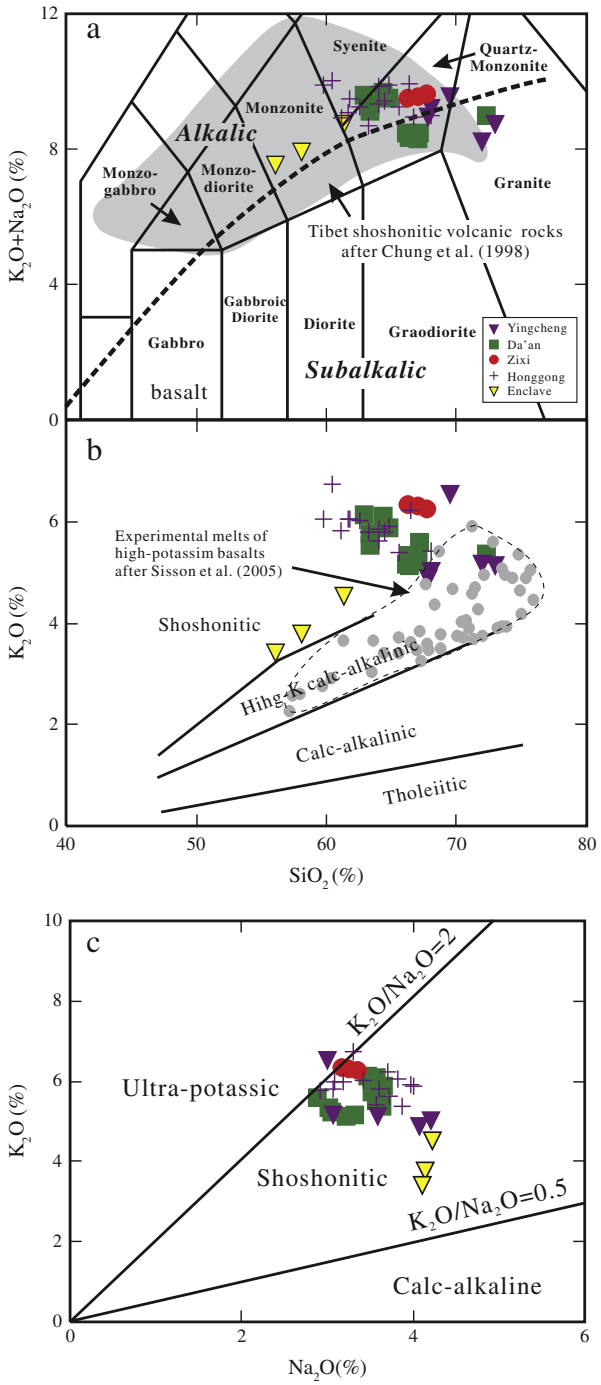

Fig. 4. (a) Total alkalic vs. SiO_2 diagram (Middlemost, 1994) for classification of the shoshonitic rocks from the northern Wuyi Mountains. The shaded area in shows shoshonitic rocks from the Tibetan Plateau after Chung et al. (1998). (b) K_2O vs. SiO_2 classification diagram of Peccerillo and Taylor (1976) showing that the studied rocks are shoshonitic in composition. The light gray dots show experimental melts from partial melting of high-K basalts after Sisson et al. (2005); (c) K_2O vs. Na_2O diagram showing that the studied rocks are dominantly shoshonitic.

from different units, they show very similar high potassium (K_2O = 3.42%–6.74%) features, with K_2O/Na_2O ratios varying from 1.19 to 2.18. With the exception of two samples (YC-4 and CF-3c) that are plotted with the ultra-potassic field, all are plotted within the shoshonitic field (Fig. 4b).

All but the enclave samples display consistent major element trends with increasing SiO_2, whereas the enclave samples generally show different trends (Fig. 5). For the non-enclave samples, the major elements

of TiO_2, Al_2O_3, FeO^t, CaO, and P_2O_5 decrease with increasing SiO_2 and show a negative correlation with SiO_2, but K_2O and Na_2O are roughly steady with increasing SiO_2, except for Honggong samples which do not show an obvious trend between FeO^t and SiO_2. The enclave samples have nearly constant Al_2O_3 and CaO contents, whereas their K_2O content increases and TiO_2, FeO^t, MgO and P_2O_5 contents decrease sharply with increasing SiO_2. Evolutionary trends of Al_2O_3, MgO, K_2O and P_2O_5 for the potassic rocks follow that of the Eocene Sunling Volcanic rocks in the Absaroka volcanic province, Wyoming (Feeley, 2003). The enclaves, on the other hand, display a mixing trend between the primitive magma and a moderately-evolved magma (Fig. 5).

Trace elements display complex behavior (Fig. 5). Zirconium concentration decreases but niobium concentration increases with increasing SiO_2 for the Da'an Yingcheng and Zixi samples. Contrarily, Zr and Nb contents of the Honggong samples quickly increase with increasing SiO_2. With the exception of sample HG-11, all samples have low Cr (4.2–18.05 ppm) and V (3.78–127.5 ppm) contents and display a weak negative correlation with SiO_2. Sample HG-11 has Cr content of 35.5 ppm higher than others. The V concentration of the enclaves decreases sharply from 127 to 68.7 ppm with increasing SiO_2 from 56.09% to 61.37%. The large ion lithophile elements (LILE, such as Ba and Sr) of all samples significantly decrease while Rb and U increase with increasing SiO_2.

The chondrite normalized REE patterns are illustrated in Fig. 6a–d. All samples display similar LREE-enriched patterns with variable negative Eu anomalies. The Da'an samples display the largest range of La/Yb_N ratios, varying from 10.7 to 36.2 and Eu anomalous values of $Eu/Eu^* = 1.06–0.19$, while the Zixi samples show the highest La/Yb_N ratios (54.5–60.2) with moderate Eu anomalies ($Eu/Eu^* = 0.47–0.56$). The La/Yb_N ratios and Eu/Eu^* values of the other samples fall between those of the Da'an and Zixi samples. Enclaves from the Yingcheng pluton show uniform LREE-enriched patterns ($La/Yb_N = 17.5–20.6$) with slightly negative Eu anomalies ($Eu/Eu^* = 0.69–0.84$). On the primitive mantle normalized trace element diagrams (Fig. 6e–h), all samples display "spiky" trace element patterns, having obvious enrichments in LILE (Rb, Th) and Pb and variable depletions in Ba, U, Sr, P, and high field strange elements (HFSE, Nb–Ta and Ti). Similar to their host-rocks, the enclaves also slightly enrich in LILE and deplete in U, P and HFSE (Nb-Ta and Ti).

4.3. Whole-rock Sr–Nd isotopes

Twenty-five whole-rock samples have been analyzed for Sr and Nd isotopic compositions, including two enclave samples (YC-1-4 and YC-1-5). The analytical results are listed in Appendix Table 3.

All samples exhibit moderate ranges of measured $^{87}Rb/^{86}Sr$ (0.69–11.90) and $^{87}Sr/^{86}Sr$ (0.709672–0.734770) ratios, corresponding to initial $^{87}Sr/^{86}Sr$ (I_{Sr}) ratios of 0.7077 to 0.7162. Among them, the Honggong samples have the largest range of I_{Sr} ratios (0.7087 to 0.7162). With the exception of two samples H-9 and H-10a (I_{Sr} = 0.7162 and 0.7134, respectively), the Honggong samples have I_{Sr} ratios focusing on from 0.7087 to 0.7162. By contrast, samples from other plutons have narrower ranges of I_{Sr} ratios within each pluton: the Zixi samples have the highest I_{Sr} ratios of 0.7112 to 0.7116; the Yingcheng (including two enclave samples) and Da'an samples have I_{Sr} ratios falling in the ranges of 0.7083–0.7091 and 0.7077–0.7091, respectively.

Similar to the Sr isotopic results, Nd isotopic compositions of the analyzed samples also display moderate variations in $^{147}Sm/^{144}Nd$ (0.067

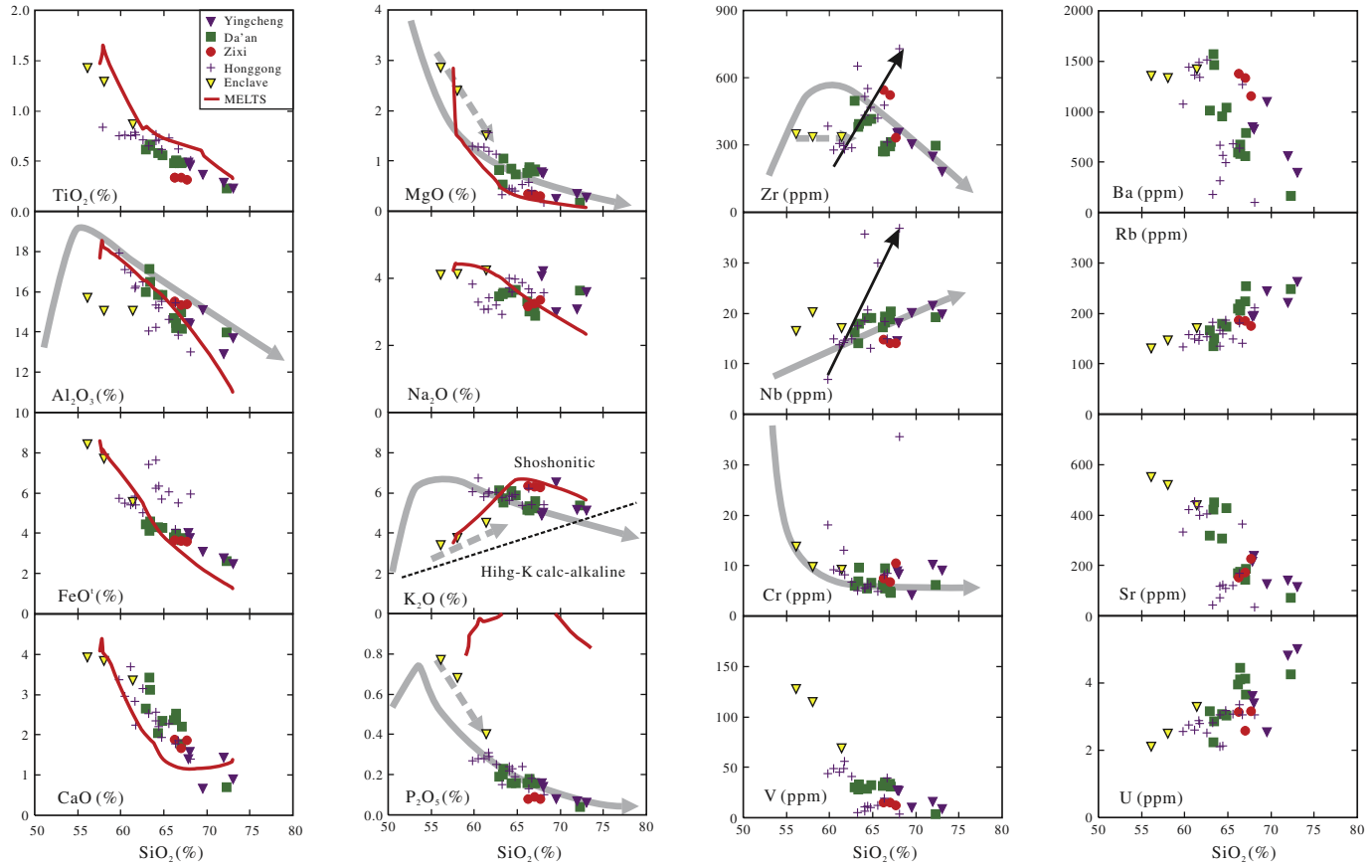

Fig. 5. Chemical variation diagrams for the shoshonitic rocks. The gray solid lines are the evolution lines for the Eocene Sunling volcanic rocks which are considered to be of a fractional crystallization origin at a shallow crustal chamber (Feeley, 2003). The gray dashed lines show the possible mixing trends. The thin lines with arrows show Zr and Nb trends of the Honggong pluton, which is different from the other plutons possible caused by fractionation of accessory minerals, such as zircon and Fe–Ti oxides.

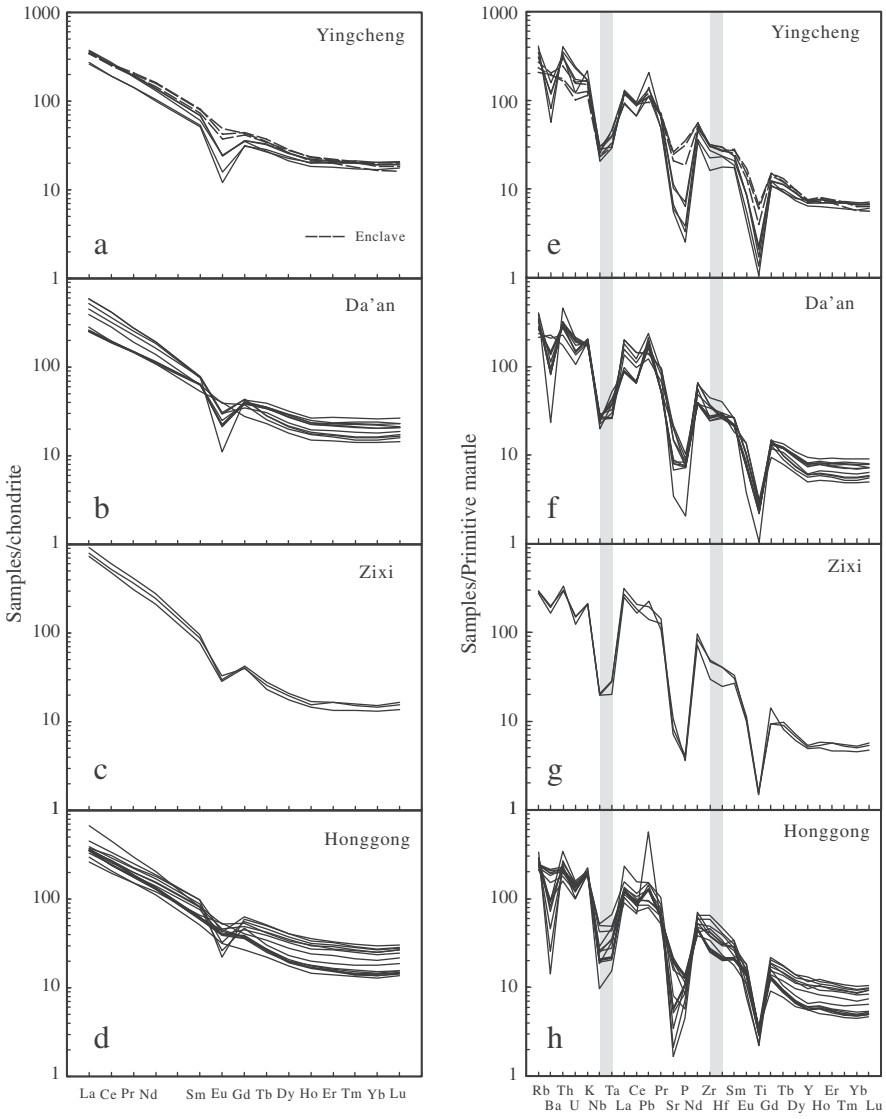

Fig. 6. Chondrite-normalized REE patterns (a–d) and primitive-mantle-normalized incompatible element spider-diagrams (e–h) for the shoshonitic rocks from the northern Wuyi Mountain.

to 0.113) and $^{143}Nd/^{144}Nd$ (0.511983 to 0.512273), corresponding to εNd(t) values of −5.6 to −10.5 and Mesoproterozoic Nd model ages (T_{DM}) of 1.12 to 1.50 Ga. Among the studied samples, the Zixi ones have the lowest $^{147}Sm/^{144}Nd$ (0.067 to 0.073) and $^{143}Nd/^{144}Nd$ (0.511983 to 0.512028) ratios, corresponding to εNd(t) values of −9.7 to −10.5, whereas the Honggong samples recorded the highest $^{147}Sm/^{144}Nd$ (0.080 to 0.109) and $^{143}Nd/^{144}Nd$ (0.512077 to 0.512273) ratios, corresponding to εNd(t) between −5.7 and −9.3. The Yingchang samples have $^{147}Sm/^{144}Nd$ of 0.098 to 0.102 and $^{143}Nd/^{144}Nd$ of 0.512038 to 0.512073, corresponding to εNd(t) values of −9.4 to −10.1 (including the εNd(t) values of −9.37 and −9.41 for the two enclave samples). The Da'an samples yielded $^{147}Sm/^{144}Nd$ of 0.082 to 0.113 and $^{143}Nd/^{144}Nd$ of 0.512088 to 0.512217, corresponding to εNd(t) values between −6.7 and −8.7 (Appendix Table 3).

4.4. Zircon Hf isotopes

Fifty-eight Hf isotope analyses were conducted on 58 zircon grains, including eleven grains from the Zixi quartz-syenite (Z-6-2), fifteen from the Yingcheng quartz monzonite (Y-1-1), eleven from the Da'an quartz monzonite (D-2-3), and twenty one from the Honggong hornblende syenite (Hong-4). The analytical results are listed in Appendix Table 4.

Most zircon grains, except seven from the Honggong pluton, were dated using the SHRIMP zircon U–Pb method before the Hf isotopic analysis. The calculated initial εHf(t) values of all samples are in the range of 2.3 to −13.1, corresponding to T_{DM} modal ages between 707 and 1330 Ma.

Among all grains, the ones from the Zixi samples have the lowest initial εHf(t) values of −8.4 to −11.5, corresponding to T_{DM} ages of 1.13 to 1.27 Ga. Both the εHf(t) values and T_{DM} modal ages of the Zixi samples show quasi-bimodal distributions averaging Hf(t) = −10 ± 0.47 (Fig. 7a) and T_{DM} = 1202 ± 23 Ma (Fig. 7b). The Honggong samples have highly variable εHf(t) values (from 2.3 to −10.4), corresponding to T_{DM} modal ages between 0.71 and 1.25 Ga. The Honggong zircons display a multi-peak distribution in εHf(t) values and T_{DM} ages (Fig. 7g, h). The initial εHf(t) of the Yingcheng samples are between that of the Zixi and Honggong samples, falling in the range of −6.4 to −10.3, corresponding to a narrow T_{DM} age range of 1.05 to 1.22 Ga. The analytical results for the Yingcheng zircons show a nearly unimodal distribution averaging εHf(t) = −8.48 ± 0.55 and T_{DM} = 1135 ± 21 Ma (Fig. 7c, d). The Da'an samples show a multi-peak distribution of εHf(t) values (−3.7 to −13.1) and T_{DM} ages (0.99 to 1.33 Ga) (Fig. 7e, f), and among the 11 zircons, seven zircons yielded a peak of εHf(t) = −7.55 ± 0.34 and T_{DM} = 1097 ± 14 Ma.

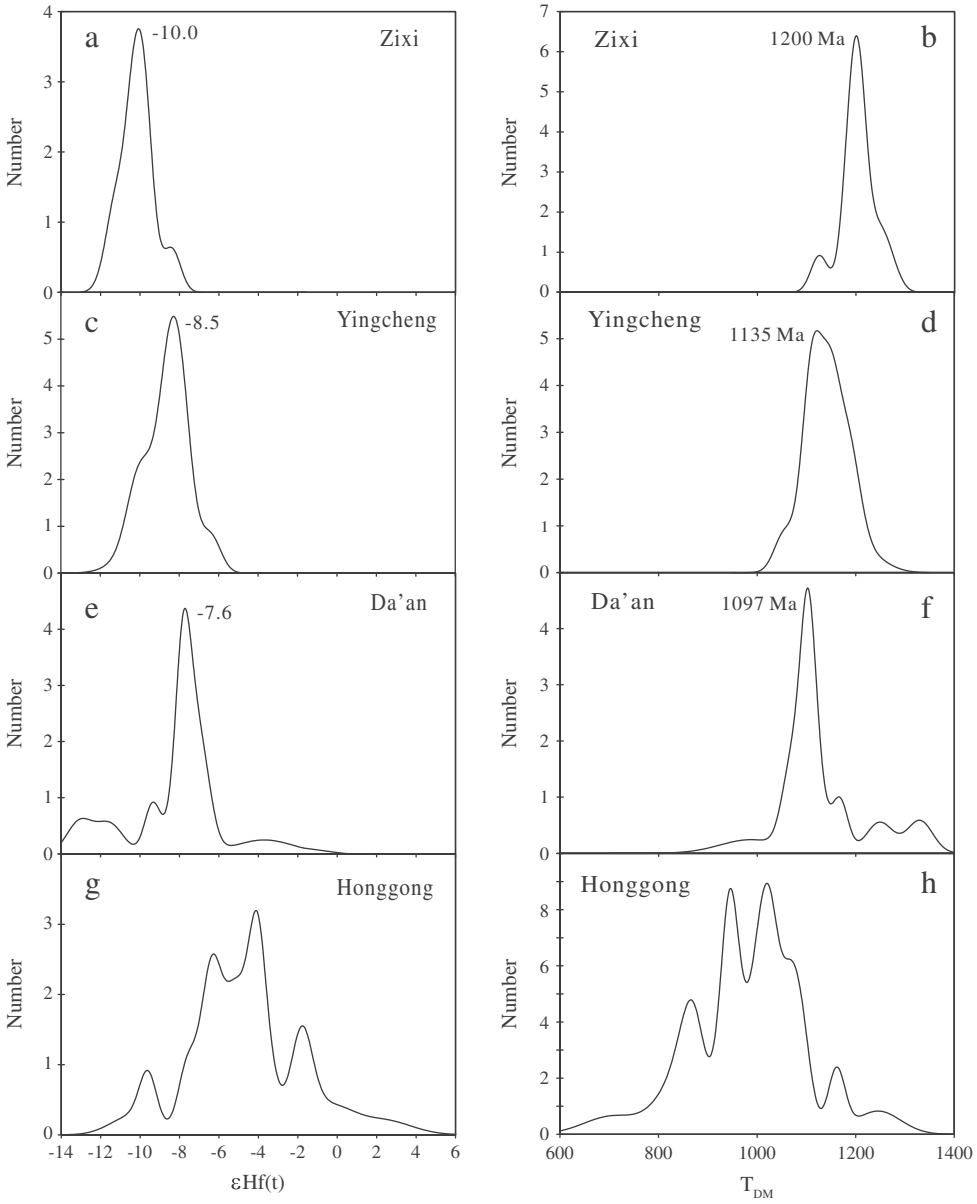

Fig. 7. Histograms of εHf(t) and Hf modal ages for the shoshonitic rocks from the northern Wuyi Mountains.

5. Petrogenesis and tectonic significance

5.1. Petrogenesis

The Early Cretaceous potassic intrusions in the northern Wuyi Mountains are metaluminous with relatively high SiO_2 (60.48–73.02%) and K_2O (3.42%–6.74%) contents, belonging to high-SiO_2 shoshonitic rocks. The high silica shoshonitic rocks can be formed by partial melting of either crustal meta-igneous and/or meta-sedimentary rocks, or metasomatized lithospheric mantle, with some extent of fractional crystallization (Campbell et al., 2014; Chung et al., 1998; Foley, 1992; Pe-piper et al., 2009; Turner et al., 1996).

The metaluminous feature (ACNK < 1) of the majority of the studied samples rules out the possibility of partial melting of metasedimentary rocks because melts derived from metasedimentary rocks are generally peraluminous (Vielzeuf and Holloway, 1988; White and Chappell, 1983). Recently, Campbell et al. (2014) put forward a new model to interpret the origin of the Tertiary high-potassic rocks of eastern Tibet. They consider that shoshonitic melts can be formed at high-T and P conditions by partial melting of the continental crust thrusted into the upper mantle by the transpressional Red River–Ailaoshan–Batan–Lijiang fault system. However, the lack of a large scale transpressional fault system in the Wuyi Mountains region during Mesozoic ruled out this possibility.

Experimental data show that partial melting of basaltic or intermediate igneous rocks can produce metaluminous to weakly peraluminous signature, but resultant granitic magmas are generally calc-alkaline to high-potassium calc-alkaline (Roberts and Clemens, 1993; Sisson et al., 2005). This is inconsistent with the shoshonitic feature of the studied rocks. Therefore, the studied samples are unlikely to be formed by partial melting of basaltic or intermediate igneous rocks. Pe-piper et al. (2009) proposed that some shoshonitic rocks could be formed by partial melting of K-enriched basaltic rocks at high pressure (1.5–2.0 GPa) and high-temperature (>950 °C) conditions. Shoshonitic rocks formed by this mechanism are expected to have geochemical feature similar to those of adakitic rocks. Adakitic rocks are characterized by high Sr/Y (>20–40) and La/Yb (>20) ratios and low Y (≦18 ppm) and Yb (≦1.9 ppm) contents due to the presence of garnet and/or amphibole residues in the source, whereas the plagioclase had been consumed (Defant and Drummond, 1993). Contrarily, our samples

have relatively high Y (>22 ppm) and Yb (>2.2 ppm) with Sr/Y ratios less than 20 (Appendix Table 2), thus, this interpretation is unlikely for the shoshonitic rocks in the northern Wuyi Mountains.

Alternatively, the northern Wuyi Mountains shoshonitic rocks are probably derived from a metasomatized subcontinental lithospheric mantle, because numerous experimental petrologic and geochemical studies indicated that partial melting of metasomatized veins in the lithospheric mantle could formed shoshonitic rocks (e.g. Chung et al., 1998; Conceicao and Green, 2004; Elkins-Tanton and Grove, 2003; Foley, 1992; Lloyd et al., 1985; Mitchell, 1995; Turner et al., 1996). Such an interpretation is also supported by the fact that the shoshonitic rocks have Sr–Nd isotopic feature similar to those of metasomatized lithospheric mantle-derived rocks, such as the Permian alkaline syenites (Wang et al., 2005) the Silurian basalts in the Cathaysia Block (Yao et al., 2012), central Italy high-K rocks (Conticelli and Peccerillo, 1992), and the South Africa kimberlites (Conticelli and Peccerillo, 1992) (Fig. 8a).

It is noted that primary melts formed by partial melting of a metasomatized lithospheric mantle are generally low in SiO_2 and high in MgO, contradicting the geochemistry of the studied shoshonitic rocks. Therefore, the crustal processes such as fractional crystallization or mixing/contamination with high-SiO_2 crustal materials should be involved in their generation. The following lines of evidence argued that such crustal processes are dominated by fractional crystallization rather than contamination: Firstly, although Sr–Nd isotopic compositions of all samples have relatively wide range ($\varepsilon Nd(t) = -5.63$ to -10.52; $I_{Sr} =$ 0.7077 to 0.7162), they are nearly constant with increasing SiO_2 in a single pluton (Fig. 8b, c). Thus, the lack of correlation between Sr–Nd isotopes and SiO_2 and Mg# indicates that crustal contamination played a minor role (Fig. 8b, c and Appendix Tables 2, 3). Therefore, the differences between different plutons may be attributed to source heterogeneity. Secondly, as shown in Fig. 5, most major elements and some trace elements plot along the trend of the Sunlight shoshonitic rocks from the Eocene Absaroka volcanic province, which was interpreted to be produced by fractional crystallization of basaltic parent magmas that were from a metasomatized lithospheric mantle (Feeley, 2003; Feeley and Cosca, 2003). Thirdly, in the V and Ni vs. Zr diagrams (Fig. 9a, b), the studied rocks follow a fractional crystallization trend (rather than a batch melting trend), suggesting that the rocks were formed by fractional crystallization of mafic parent magmas. In addition, the rocks have significantly lower contents of Ni (1.13–18.32 ppm) and V (4.93–55.88) (Fig. 9a,b), which are even lower than their respective upper crustal abundances (Ni = 20 ppm, V = 60 ppm, Rudnick and Fountain, 1995), the possibility of mixing/contaminating of basaltic magmas with crustal material, thus, can be ruled out. Lastly, the studied enclave samples plot along a mixing trend between primitive or intermediate evolved rocks and highly evolved felsic rocks (Fig. 5), suggesting a possible mixing origin. These enclave samples have potassium contents significantly lower than those of the host rocks (Fig. 5), implying that the high-K host rocks are unlikely to be produced by magma mixing. The bivariate figures of major and trace elements can be used to estimate fractionated mineral assemblage (Janoušek et al., 2004; Li et al., 2007). As shown in Fig. 10a and b, positive and relatively flat linear correlations of Sr vs. Ba and Sr vs. Rb suggest that K-feldspar and/or plagioclase are the major phases in the assemblage of fractional minerals. This is supported by variable Eu/Eu* negative anomalies in the REE patterns (Fig. 6a–d), and significant Sr anomaly relative to neighboring elements in the trace element spider-diagrams (Fig. 6e–g). The obvious P and Ti negative anomalies in the spider-diagrams (Fig. 6e–g) indicate that both apatite and Fe–Ti oxides are involved in the assemblage fractional mineral.

In order to further determine possible crystallization condition, particularly pressure, water content and oxygen fugacity, we performed simulation using the Rhyolite-MELTS software (Gualda et al., 2012). The least-evolved sample of YC1-5 was chosen as the starting material, and the simulation conditions are 1.5% water, 1.5 kbar pressure and FQM-1 oxygen fugacity (Fig. 5). The results fit well with the studied

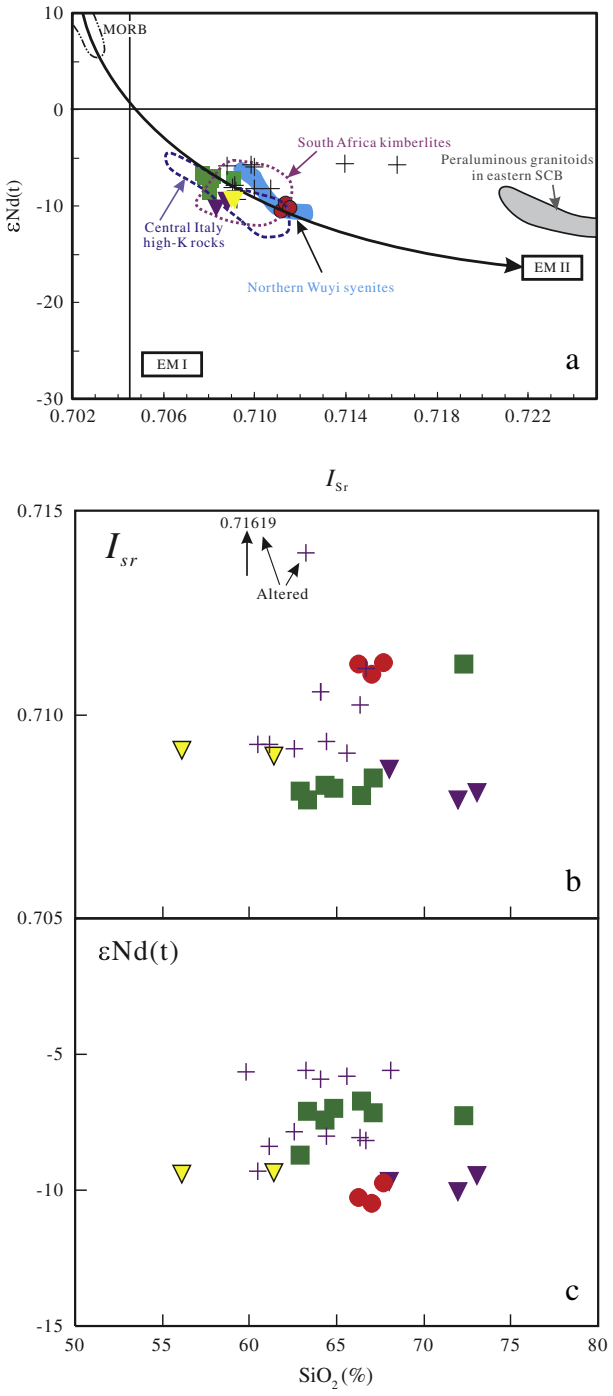

Fig. 8. (a) Initial εNd(t) vs. I_{Sr} diagram for the shoshonitic rocks of the northern Wuyi Mountains. The data of ~240 Ma alkaline syenite and peraluminous granitoids in eastern SCB are from Wang et al. (2005); data for the central Italy high-K rocks and South Africa kimberlite are after Conticelli and Peccerillo (1992); SiO_2 vs. I_{Sr} (b) and εNd(t) (c) variation diagrams show small variations within a single pluton but there are obvious differences between plutons. Symbols are as in Fig. 5.

rocks, except for P_2O_5 (Fig. 5), and the Al_2O_3 and MgO versus SiO_2 variation broadly matches the trends of Sunlight shoshonitic rocks from the Eocene Absaroka volcanic province (Feeley, 2003; Feeley and Cosca, 2003). The modal crystallization mineral assemblage shows in Fig. 11. Due to SiO_2 content of the studied rocks being dominant between ~62% and 70% (gray area in Fig. 11), the major crystallization mineral phases are potassium feldspar and plagioclase, as well as minor Fe–Ti oxides and apatite in this area. The modal mineral assemblage is consistent with the geochemical observation above. The exception is that

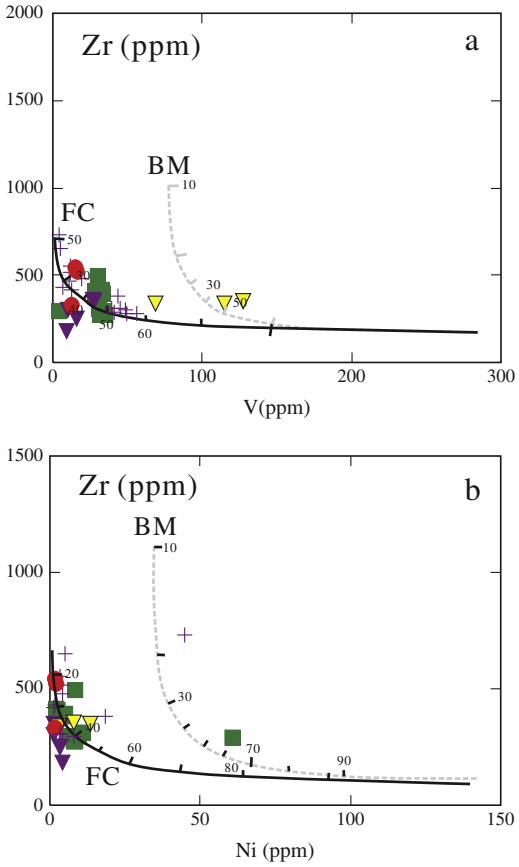

Fig. 9. (a) V and (b) Ni vs. Zr diagrams showing that fractionation rather than batch melting is favored for the origin of the shoshonitic rocks of the northern Wuyi Mountains. Symbols are as in Fig. 5.
(After Peccerillo et al. (2003)).

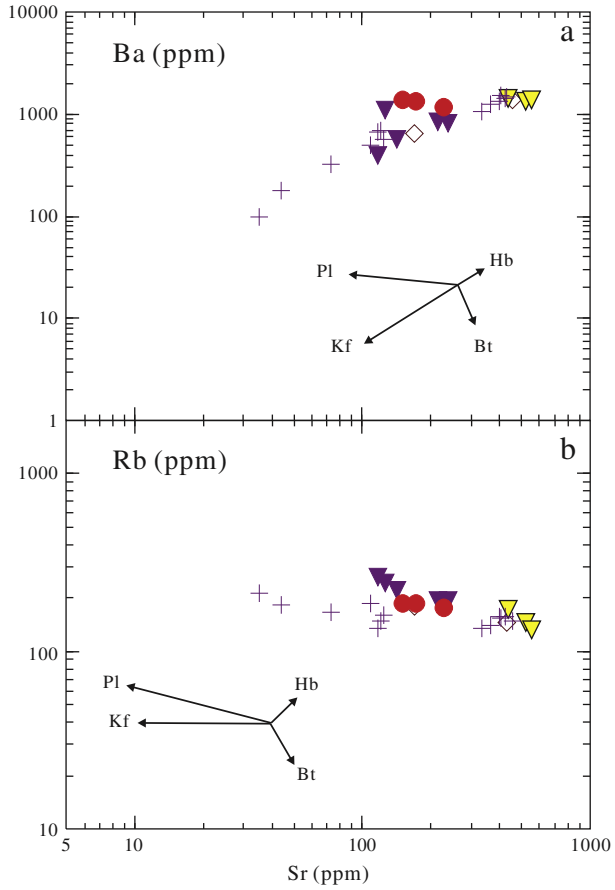

Fig. 10. (a) Ba and (b) Rb vs. Sr diagrams showing K-feldspar and plagioclase-dominated fractional crystallization in the shoshonitic rocks from the northern Wuyi Mountains. Symbols are as in Fig. 5.

minor olivine, rather than amphibole and/or biotite which are main ferromagnesian minerals observed in the studied rocks, appears as the main ferromagnesian mineral, probably because of lack of appropriate thermodynamic models for hydrous mafic silicates, particularly amphibole and biotite for wet intermediate rocks (Gualda et al., 2012).

Therefore, the northern Wuyi Mountains shoshonitic rocks were most likely derived from an enriched lithospheric mantle source and then underwent fractional crystallization at low pressure (1.5 kbar), involving a mineral assemblage of dominant K-feldspar, plagioclase and accessory minerals apatite and Fe–Ti oxides, while the crustal mixing/contamination plays a minor role.

5.2. Tectonic significance

5.2.1. Potassic magmatism as an indicator for the onset of eastward roll-back of a flat-slab?

The detailed geochemical features of the Cretaceous shoshonitic rocks from the northern Wuyi Mountains indicate that they are most likely derived from a metasomatized subcontinental mantle. The underlying question then is: what mechanism caused the partial melting of the subcontinental lithospheric mantle at ca. 500 km away from the trench (probably present eastern margin of Taiwan)? Many researchers propose Cretaceous (arc) magmatism in South China formed by the westward subduction of the Paleo-Pacific Plate beneath the eastern margin of the Eurasia continent (He and Xu, 2012; Jahn et al., 1976; Lan et al., 1996; Lapierre et al., 1997; Li and Zhou, 2000; J.H. Li et al., 2014; Z. Li et al., 2014; L. Li et al., 2014; Martin et al., 1994; Zhou and Li, 2000). However, such arc-related magmas are generally produced in a narrow region of about 250–300 km away from the trench under normal subduction angles (English et al., 2003; Gutscher et al., 2000). If arc-related magmatism truly occurs over 500 km inboard from the trench, the most probable is either shallow angle- or flat-subduction, similar to the late Cretaceous to early Cenozoic North American Cordillera, where flat/shallow subduction forms a magmatic arc beneath Colorado Plateau away from trench over 500 km (Erdman et al., 2016; Lee, 2005; Saleeby, 2003; Smith, 2013). However, the coeval arc-related magmatic rocks did exist along the coastal region of SE South China since ca. 190 Ma and last until ca. 90 Ma (Z.X. Li et al.,

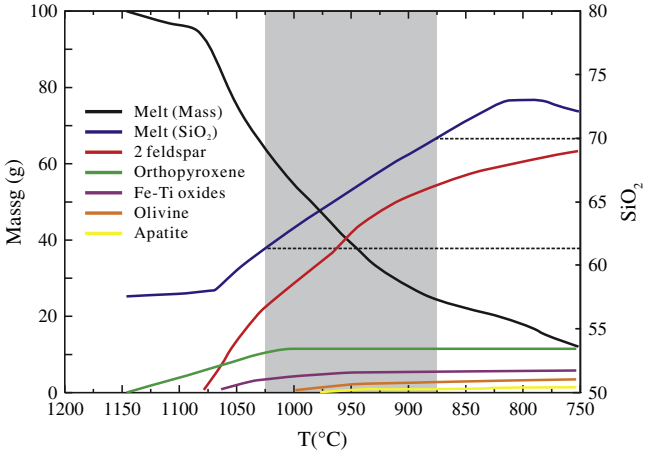

Fig. 11. Rhyolite-MELTS simulation shows melt mass, SiO_2 content and mineral crystallization sequence with temperature. The starting material is YC1-5.

2012), and their geochemical characteristic is dominantly high-K calc-alkaline (J.H. Li et al., 2014; Z. Li et al., 2014; L. Li et al., 2014; Sewell and Campbell, 1997), distinct from the Cretaceous shoshonitic rocks studied here, thus, the interpretation related directly to subduction can be ruled out. A flat-subduction model has indeed been suggested for Mesozoic South China (Li and Li, 2007). According to this model, an oceanic plateau underwent flat-subduction between ca. 250 and 200 Ma. Delamination and/or roll-back of the flat-slab started from the hinterland at late Triassic/early Jurassic and the coastal fragment of the flat slab rolled-back toward the trench during the Jurassic–Cretaceous time. This model predicts the arrival of the slab roll-back at the northern Wuyi Mountains region by ca. 140 Ma (Fig. 14b). According to the flat-slab model, the earlier subducted flat-slab rolled back eastward off the bottom of the subcontinental lithospheric mantle (Li and Li, 2007), caused asthenospheric mantle upwelling and thus triggered partial melting of the metasomatized lithospheric mantle to produce shoshonitic rocks in the northern Wuyi Mountains. Such an interpretation is also consistent with the coastward-younging trend of the Cretaceous magmatism in southeastern China (Li and Li, 2007; Z.X. Li et al., 2012; J.H. Li et al., 2014; Z. Li et al., 2014; Zhou and Li, 2000).

5.2.2. Early Mesozoic subduction affects the South China subcontinental lithospheric mantle

The influence of the early Mesozoic subduction system in South China is an important, but still controversial issue. Based on the geochemistry of Mesozoic mafic rocks in South China, Chen et al. (2008) suggested that the subduction effect was limited in the coastal region, but not as far interior as the Wuyi Mountains region, implying a normal-angle subduction system during Early Mesozoic. Here, the high-potassic rocks derived from the subcontinental lithospheric mantle (SCLM; He et al., 2008; X.H. Li et al., 2003; Li et al., 2004a; Wang et al., 2005) provide a good opportunity for us to re-evaluate the lateral extent of subduction modification to the SCLM of Mesozoic South China. Since the high-potassic rocks are widespread in South China, particularly in the Wuyi Mountains and the South China interior (Fig. 1a), we selected seven Mesozoic shoshonitic and high-potassic alkaline intrusive and volcanic rocks in the Wuyi Mountains region and South China interior to evaluate the influence of Mesozoic subduction (Fig. 12).

Before this work, the pre-Mesozoic orogenic effect should be discussed. There are two possible subduction events which affect the South China Block before Mesozoic, i.e. early Neoproterozoic Sibao orogeny and early Paleozoic Wuyi–Yunkai orogeny (Li et al., 2009, 2010; Ye et al., 2007). Numerous studies show that after Sibao and Wuyi–Yunkai orogenies, voluminous mafic and felsic igneous rocks are widespread over eastern South China Block, especially in Cathaysia Block (Li et al., 2003, 2005, 2009). Subsequently, Neoproterozoic rift (Nanhua rift, Wang and Li, 2003) and early Paleozoic lithospheric delaminating (Li et al., 2010; Yao et al., 2012) follow these magmatic events. Therefore, we infer that early metasomatic rocks produced in the subcontinent lithospheric mantle are difficult to retain after the intensive magmatic thermal events.

The selected rocks are, from east to west, Indosinian alkaline syenites (Wang et al., 2005), the northern Wuyi shoshonitic rocks (this study), the Huichang shoshonitic volcanic rocks (He et al., 2008), the Ejinao alkaline rocks (Bao et al., 2000), the Quannan syenites (XH Li et al., 2003), the Lisong shoshonitic rocks (Zhu et al., 2006) and the Tong'an and Niumiao shoshonitic rocks (Zhu et al., 2005). On the diagram of εNd(t) vs. La/Nb ratio (Fig. 13a), the rocks from the South China interior, such as the E'jinao, S Jiangxi, Lisong, Tong'an and Niumiao plutons, display a linear distribution between the mantle array and South China SCLM, with the highest La/Nb ratios more than 1. This suggests a weak subduction influence while dominantly time-depended enrichment of the Nd isotope. In contrast, the rocks from the Wuyi Mountains region, including the Indosinian syenite (Wang et al., 2005), the shoshonitic rocks reported here, and the Huichang

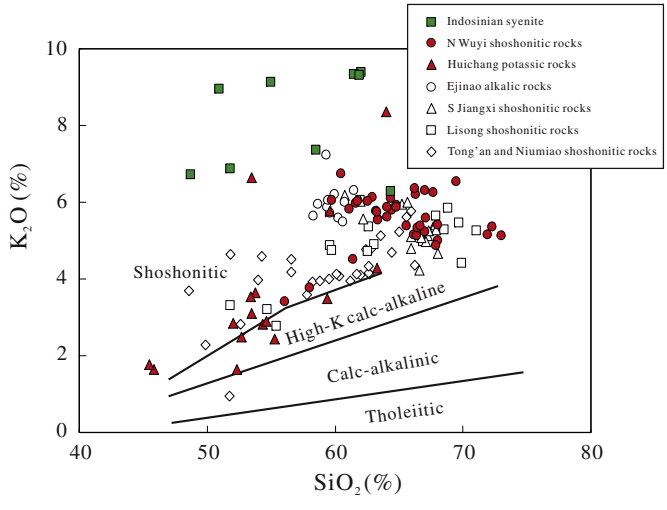

Fig. 12. A K_2O vs. SiO_2 diagram showing the shoshonitic character of the Mesozoic potassic rocks in the Wuyi Mountains and the South China interior. Data sources: Indosinian alkaline syenite (Wang et al., 2005); northern Wuyi Mountains shoshonitic rocks (this study); the Huichang shoshonitic rocks (He et al., 2008); the Ejinao alkaline rocks (Bao et al., 2000); Southern Jiangxi shoshonitic rocks (Li et al., 2003); the Lisong shoshonitic rocks (Zhu et al., 2006); the Tong'an and Niumiao shoshonitic rocks (Zhu et al., 2005).

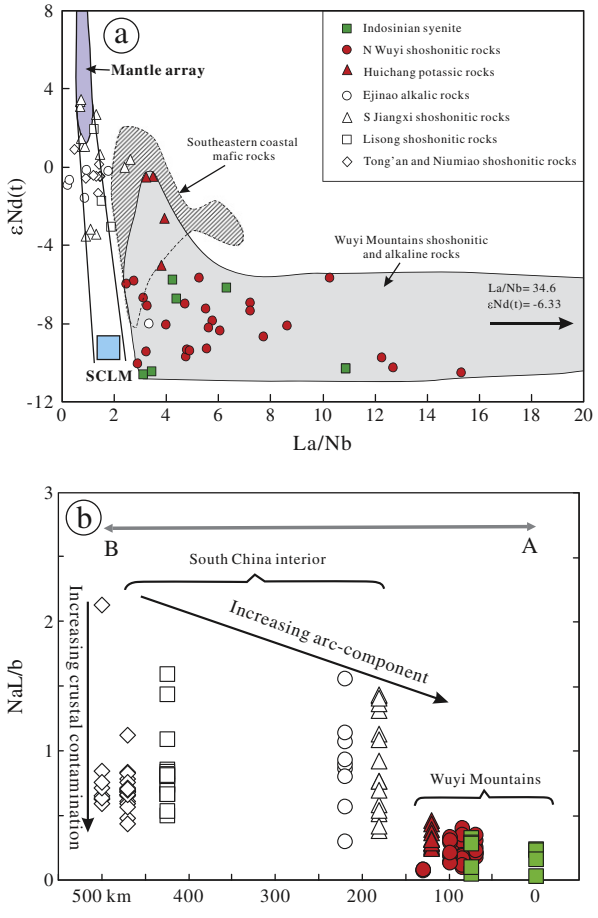

Fig. 13. (a) εNd(t) vs. La/Nb diagram shows that samples from the Ejinao alkaline rocks, the southern Jiangxi shoshonitic rocks, the Lisong shoshonitic rocks and the Tong'an and Niumiao shoshonitic rocks plot between the mantle array and the South China lithospheric mantle, suggesting a lack subduction influence, whereas the Indosinian syenites, the northern Wuyi Mountains shoshonitic rocks and the Huichang shoshonitic rocks have high La/Nb ratios, implying variable subduction influences (after Chen et al., 2008). (b) Variation in the Nb/La ratios between difference regions with low Nb/La samples coming from the Wuyi Mountains whereas high Nb/La samples coming from the South China interior.

shoshonitic rocks (He et al., 2008), show obvious arc-signatures with a variable Nb/La ratio of less than 0.5 (Fig. 13a). The notable declining Nb/La ratios from west to east (Fig. 13b) suggest that subduction influence was probably limited in the Wuyi Mountains region, about 500 km away from the trench, while it dramatically decreases further west to the interior of the South China (west of the Wuyi Mountains). Such a ~500 km-wide subduction-affected zone implies a low-angle (Zhou and Li, 2000) or flat (Li and Li, 2007) subduction (English et al., 2003; Gutscher et al., 2000; Sommer and Gauert, 2011). Meng et al. (2012) studied Mesozoic basalts from South China, and obtained a similar conclusion that the influence of subduction was weak in the continental interior (west of the Wuyi Mountains) during the early Mesozoic.

Here, we illustrated the petrogenesis of the shoshonitic rocks in the northern Wuyi Mountains (Fig. 13), according to Li and Li (2007) proposed tectonic model and our new results. (1) The initial subduction probably began at ~280 Ma as evidenced by ~270 Ma calc-alkaline I-type granites in Hainan Island and a detrital zircon age peak of ~280 Ma from the Middle to Late Permian sediments in southeastern China (X.H. Li et al., 2006, 2012). The arrival of a buoyant oceanic plateau at around 250 Ma started to flatten the subducting slab, broadening the subduction-modified SCLM (marked as MLM in Fig. 14a) further inland to the Wuyi Mountains region. The subduction influence probably reached the Wuyi Mountains region, ~500–600 km away from the trench. (2) At Cretaceous (ca. 140 Ma), the flat slab rolled-back toward the east, resulting in eastward-younging of the Cretaceous magmatism in the Wuyi Mountain region and coastal zone of southeastern China (Li and Li, 2007; Z.X. Li et al., 2012; Zhou and Li, 2000). The roll-back of the flat-slab caused asthenospheric mantle upwelling and triggered partial melting of the metasomatized lithospheric mantle above it and produced the early Cretaceous shoshonitic magmatism in the northern Wuyi Mountains (Fig. 14b).

6. Conclusion

SHRIMP zircon U–Pb dating results indicate that shoshonitic rocks in the northern Wuyi Mountains occurred at 139–126 Ma. These Early Cretaceous shoshonitic rocks are characterized by high-SiO_2 and potassium contents. Their geochemical features suggest that the rocks were derived from an enriched subcontinental lithospheric mantle. These rocks underwent significant fractional crystallization involving mainly K-feldspar, plagioclase, and accessory, such as mineral apatite and Fe–Ti oxides, during ascent. They are likely formed during the roll-back of the early Mesozoic subducted flat-slab, representing the onset of the Cretaceous magmatism in South China. A review of the geochemical results of lithospheric-mantle-derived potassic rocks in South China reveals that influence of the Mesozoic subduction system had probably reached the Wuyi Mountains region, ca. 500–600 km away from the trench. Both the broad metasomatized zone in the subcontinental lithospheric mantle, and the occurrence of the shoshonitic intrusions in the Early Cretaceous at northern Wuyi Mountains, imply a shallow (flat) subduction at Early Mesozoic in South China.

Acknowledgments

We are extremely grateful to Zheng-Xiang Li (Curtin University) for his constructive suggestion and fruitful discussion, Y. Liu, X. L. Tu, and X. R. Liang for their assistance in geochemical and Nd isotopic analyses, and B. Song and H. Tao for assistance with the SHRIMP U–Pb zircon analyses. F.S. Lou and Z.Z. Huang are thanked for helping in the field. Comments and suggestions from Dr. Greg Shellnutt and an anonymous reviewer and editor in-chief Sun-Lin Chung greatly improved the paper. This work was supported by the National Key Research and

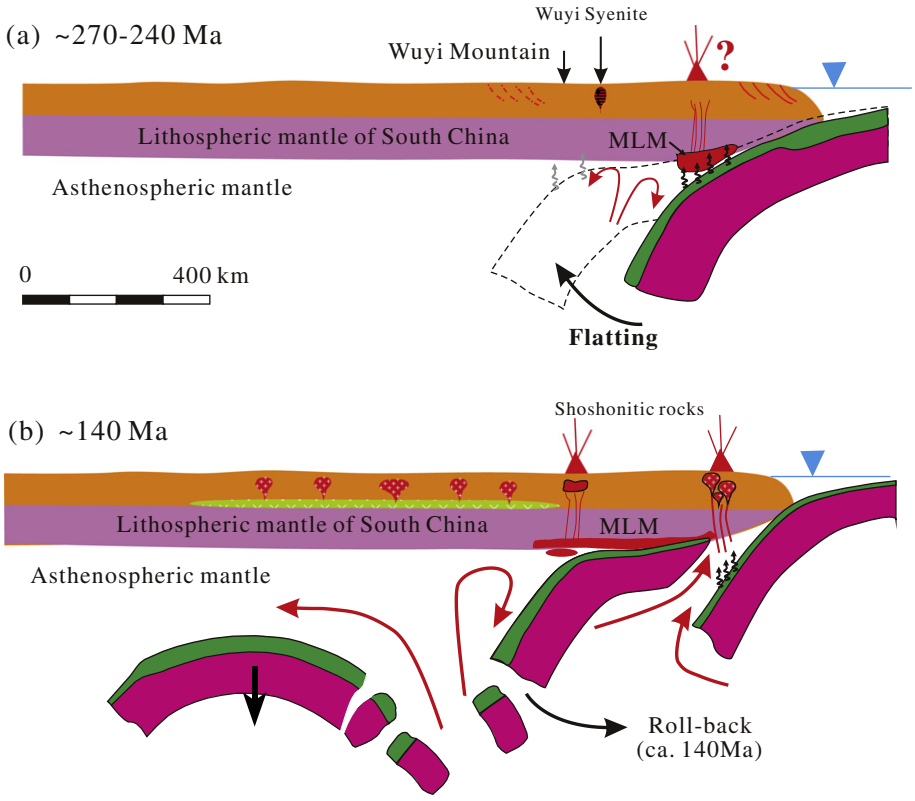

Fig. 14. A cartoon showing the Mesozoic tectonic evolution of the southeastern China and the formation of the shoshonitic rocks in the northern Wuyi Mountains region as responded to the roll-back of the shallow or flat slab (modified from Li and Li, 2007; Z.X. Li et al., 2012). MLM—metasomatized lithospheric mantle.

Development Program of China (2016YFC0600204), National Natural Science Foundation of China (grants 41373033, 41173039 and 41573026), and ARC Future Fellowship (FT140100826) and the Fundamental Research Funds for the Central Universities (program for Innovative Research Team of chemical geodynamics and Earth resources: 310827163412) to X.C. Wang. This is GIGCAS contribution No. IS-2403.

Appendix A

Appendix Table 1
SHRIMP U–Pb zircon data of shoshonitic rocks from the northern Wuyi Mountains.

Grain	U (ppm)	Th (ppm)	Th/U	f_{206} (%)	$^{207}Pb^*/^{235}U^*$ (±1σ)		$^{206}Pb^*/^{238}U$ (±1σ)		$^{206}Pb/^{238}U$ age (Ma) (±1σ)	
Y-1-1										
1.1	166	139	0.84	3.63	0.174	0.013	0.0223	0.0011	142.0	6.9
2.1	252	211	0.84	5.32	0.117	0.011	0.0207	0.0004	132.4	3.4
3.1	325	339	1.04	2.79	0.170	0.009	0.0215	0.0004	136.8	3.4
4.1	179	182	1.02	2.62	0.136	0.028	0.0214	0.0005	136.6	3.9
5.1	173	140	0.81	3.67	0.137	0.017	0.0205	0.0005	131.0	3.6
6.1	297	266	0.90	1.48	0.136	0.011	0.0215	0.0004	136.9	3.3
7.1	330	223	0.68	2.53	0.150	0.012	0.0207	0.0004	132.3	2.9
8.1	309	352	1.14	2.06	0.134	0.009	0.0209	0.0007	133.5	6.0
9.1	582	346	0.59	0.90	0.145	0.006	0.0205	0.0004	131.0	2.7
10.1	141	140	0.99	6.86	0.173	0.016	0.0217	0.0005	138.3	4.2
11.1	135	119	0.88	8.14	0.087	0.025	0.0192	0.0009	122.8	8.1
12.1	468	297	0.63	0.86	0.171	0.006	0.0222	0.0004	141.8	2.9
13.1	287	214	0.75	1.90	0.138	0.018	0.0208	0.0004	133.0	3.2
14.1	99	151	1.53	3.86	0.169	0.028	0.0204	0.0005	130.0	5.5
15.1	299	240	0.80	2.37	0.133	0.012	0.0205	0.0007	130.6	5.1
Weighted mean (2σ) (n = 15)									**134.4**	**2.3**
Z-6-2										
1.1	528	428	0.81	0.42	0.153	0.008	0.0211	0.0004	134.4	2.5
2.1	243	323	1.33	1.75	0.165	0.020	0.0213	0.0005	135.6	3.3
3.1	171	141	0.82	4.83	0.120	0.039	0.0215	0.0006	137.2	3.6
4.1	227	249	1.10	2.98	0.130	0.025	0.0207	0.0005	132.1	3.2
5.1	134	112	0.84	3.07	0.165	0.034	0.0220	0.0007	140.5	4.3
6.1	538	461	0.86	1.14	0.135	0.010	0.0216	0.0004	137.9	2.4
7.1	60	44	0.73	7.36	0.163	0.065	0.0197	0.0008	125.8	5.2
8.1	146	115	0.79	3.13	0.152	0.031	0.0214	0.0005	136.2	3.4
9.1	228	287	1.26	2.27	0.159	0.022	0.0216	0.0005	137.5	3.1
10.1	129	87	0.67	3.84	0.142	0.032	0.0211	0.0005	134.5	3.4
11.1	589	476	0.81	1.02	0.139	0.010	0.0218	0.0004	138.7	2.5
12.1	469	562	1.20	1.91	0.128	0.022	0.0216	0.0004	138.0	2.7
Weighted mean (2σ) (n = 11)									**136.6**	**1.8**
D-2-3										
1.1	414	322	0.78	2.70	0.128	0.008	0.0219	0.0004	139.7	3.1
3.1	406	216	0.53	1.05	0.153	0.009	0.0220	0.0004	140.5	3.0
4.1	421	284	0.67	3.01	0.165	0.009	0.0228	0.0004	145.6	3.2
5.1	91	103	1.13	3.41	0.167	0.037	0.0237	0.0009	150.9	7.9
6.1	107	72	0.67	3.63	0.162	0.024	0.0223	0.0006	142.0	5.2
7.1	1005	814	0.81	0.46	0.152	0.005	0.0225	0.0004	143.5	3.0
8.1	381	248	0.65	2.32	0.133	0.006	0.0204	0.0004	129.9	2.8
9.1	273	226	0.83	3.83	0.151	0.010	0.0213	0.0004	135.7	3.4
10.1	187	225	1.20	3.91	0.128	0.023	0.0212	0.0005	135.3	4.4
11.1	750	1525	2.03	1.13	0.164	0.009	0.0222	0.0004	141.3	3.9
Weighted mean (2σ) (n = 11)									**139.3**	**3.9**
H-4										
1.1	539	519	0.96	−0.03	0.129	0.005	0.0191	0.0003	121.7	2.1
2.1	344	402	1.17	−0.50	0.137	0.008	0.0193	0.0004	123.2	2.2
3.1	274	201	0.73	1.01	0.116	0.009	0.0212	0.0004	135.4	2.5
4.1	516	441	0.85	−0.23	0.146	0.008	0.0205	0.0004	130.5	2.3
5.1	241	268	1.11	0.08	0.130	0.010	0.0190	0.0004	121.2	2.3
6.1	334	261	0.78	0.12	0.137	0.007	0.0200	0.0004	127.8	2.3
7.1	167	195	1.17	−0.57	0.152	0.011	0.0201	0.0004	128.5	2.5
8.1	126	151	1.20	3.02	0.074	0.017	0.0185	0.0004	118.3	2.5
9.1	316	389	1.23	0.19	0.121	0.008	0.0195	0.0004	124.6	2.3
10.1	157	174	1.11	2.22	0.108	0.019	0.0193	0.0004	123.3	2.6
11.1	490	449	0.92	0.36	0.139	0.006	0.0208	0.0004	133.0	2.3
12.1	810	1054	1.30	0.35	0.122	0.005	0.0194	0.0003	123.7	2.1
13.1	111	123	1.11	2.14	0.087	0.027	0.0192	0.0005	122.9	2.9
14.1	303	358	1.18	3.08	0.147	0.024	0.0197	0.0004	125.7	2.5
Weighted mean (2σ) (n = 14)									**125.7**	**2.7**

The underlined datum is excluded in age calculation.

Appendix Table 2
Major and trace elements results of shoshonitic rocks from the northern Wuyi Mountains.

	YC-1-1	YC-1-2	YC-1-3*	YC-1-4*	YC-1-5*	YC-1-6	YC-3a	YC-4	HG-4	HG-5	HG-6	HG-7	HG-8	HG-9	HG-10a	HG-11	DA-1	DA-2-1	DA-2-2a	DA-2-3
Major oxides (%)																				
SiO_2	68.00	67.87	58.04	61.37	56.09	73.02	71.96	69.51	64.44	64.05	65.58	64.04	64.78	59.76	63.21	68.06	72.32	67.05	66.19	66.41
TiO_2	0.45	0.49	1.29	0.87	1.43	0.23	0.29	0.37	0.72	0.70	0.73	0.77	0.62	0.75	0.65	0.51	0.23	0.48	0.48	0.51
Al_2O_3	14.38	14.46	15.07	15.07	15.70	13.68	12.92	15.10	15.19	15.35	14.62	14.23	15.53	17.93	14.04	13.02	13.97	14.99	14.69	14.19
FeO	3.76	4.00	7.71	5.56	8.42	2.49	2.76	3.08	6.33	6.23	6.06	7.62	5.69	5.74	7.41	5.96	2.63	3.77	3.80	3.99
MnO	0.07	0.07	0.16	0.13	0.15	0.05	0.06	0.05	0.13	0.14	0.13	0.18	0.12	0.10	0.14	0.14	0.04	0.06	0.07	0.07
MgO	0.75	0.77	2.40	1.51	2.85	0.27	0.35	0.25	0.45	0.45	0.53	0.40	0.41	1.29	0.33	0.17	0.17	0.79	0.76	0.87
CaO	1.57	1.40	3.83	3.36	3.93	0.89	1.44	0.67	2.21	2.57	2.27	2.34	1.94	3.37	2.53	1.40	0.71	1.78	2.36	2.53
Na_2O	4.21	4.07	4.13	4.23	4.11	3.59	3.07	3.00	3.60	4.00	3.87	3.72	3.97	3.82	2.92	3.57	3.63	3.05	3.31	3.22
K_2O	5.01	4.88	3.78	4.52	3.42	5.13	5.16	6.54	5.80	5.86	5.38	5.62	5.92	6.06	5.78	5.42	5.37	5.23	5.15	5.14
P_2O_5	0.14	0.16	0.68	0.40	0.77	0.06	0.07	0.08	0.23	0.22	0.24	0.24	0.19	0.27	0.15	0.10	0.04	0.16	0.16	0.18
LOI	1.65	1.81	2.94	2.99	3.06	0.55	1.93	1.41	0.85	0.41	0.59	0.79	0.75	0.79	2.73	1.65	0.87	2.64	2.94	2.94
Total	100.01	99.98	100.02	100.01	99.94	99.97	100.01	100.06	99.95	99.99	99.99	99.95	99.93	99.89	99.90	100.00	99.99	99.99	99.90	100.05
ACNK	0.95	1.00	0.84	0.84	0.89	1.05	0.98	1.14	0.94	0.87	0.90	0.86	0.94	0.94	0.90	0.91	1.07	1.08	0.96	0.92
Trace elements (ppm)																				
V	26.8	27.6	114	68.7	127	8.98	16.0	9.96	11.8	11.2	12.4	6.72	10.3	43.6	4.93	4.02	3.78	33.5	31.8	35.1
Cr	8.34	8.88	9.83	9.15	13.79	9.12	10.15	4.20	6.32	5.66	4.85	5.53	5.87	18.1	5.02	35.5	6.17	4.84	6.15	9.49
Co	4.64	4.84	14.0	9.27	15.6	1.85	2.97	2.41	3.02	2.49	3.21	2.22	2.35	6.52	1.12	1.24	1.22	4.35	4.31	4.88
Ni	7.71	1.13	3.43	2.87	13.41	4.27	3.21	1.31	3.32	4.10	1.29	1.66	17.5	18.3	4.74	44.8	9.51	60.8	7.96	8.22
Ga	18.9	19.1	20.5	19.6	21.0	18.4	17.2	20.2	25.8	25.7	25.2	27.0	24.7	18.5	26.9	28.4	19.9	19.3	19.1	18.8
Ge	1.13	1.19	1.55	1.60	1.44	1.45	1.39	1.37	1.66	1.77	1.51	1.43	1.67	1.39	2.13	1.98	1.67	1.29	1.38	1.37
Rb	195	194	147	171	131	262	221	244	159	135	149	167	186	134	182	211	248	224	209	205
Sr	238	216	519	438	550	116	142	126	124	117	121	73.0	109	334	44.3	35.2	72.1	145	169	176
Y	32.8	32.8	34.1	34.4	31.5	33.9	31.4	29.2	48.8	40.3	44.4	52.7	47.4	25.7	54.8	60.1	43.2	36.3	34.7	35.7
Zr	357	352	337	337	349	183	250	304	553	515	420	431	466	384	651	730	298	294	273	273
Nb	18.1	14.6	20.3	17.0	16.5	19.9	21.5	20.1	20.7	18.5	30.0	35.7	13.1	6.88	17.5	36.8	19.2	18.8	17.2	19.4
Cs	5.07	4.95	6.96	4.73	8.52	3.84	6.23	5.83	1.96	1.51	2.38	5.49	2.44	2.07	1.65	3.53	3.05	8.06	5.85	5.42
Ba	825	848	1336	1421	1358	397	563	1096	564	671	681	320	498	1072	179	99.1	163	561	593	582
La	86.0	85.9	81.6	81.3	81.0	64.5	62.2	89.5	83.0	62.1	82.7	88.7	77.8	70.7	92.0	107	106	61.2	59.1	60.8
Ce	161	161	161	154	158	118	118	168	157	120	169	188	149	127	177	204	197	119	115	119
Pr	18.3	18.4	19.9	18.4	19.1	13.5	13.6	17.8	18.8	14.4	19.1	21.7	17.5	14.4	20.9	23.7	22.1	14.2	13.9	14.3
Nd	64.5	65.7	75.4	68.6	74.2	46.4	49.0	60.8	70.6	56.3	72.0	83.7	64.7	51.6	79.1	88.3	76.2	52.5	51.1	53.5
Sm	10.5	10.5	12.5	11.3	12.1	7.78	8.17	9.23	12.4	10.2	12.7	15.1	11.6	7.91	13.6	15.0	11.8	9.79	9.48	9.74
Eu	1.39	1.41	2.48	2.19	2.83	0.70	0.92	1.41	2.67	3.11	3.03	2.45	2.30	1.84	1.88	1.29	0.64	1.25	1.28	1.24
Gd	7.32	7.43	9.01	8.50	8.95	6.53	6.32	7.29	10.1	8.38	11.1	13.0	9.20	5.44	11.4	12.2	8.71	8.16	7.87	8.08
Tb	1.21	1.23	1.41	1.29	1.32	1.00	1.08	1.01	1.59	1.29	1.57	1.92	1.47	0.83	1.72	1.88	1.46	1.33	1.28	1.28
Dy	6.54	6.68	7.24	7.14	6.66	5.73	5.95	5.44	8.99	7.06	8.58	10.4	8.26	4.46	9.55	10.2	8.09	7.26	7.00	7.32
Ho	1.25	1.24	1.31	1.33	1.21	1.15	1.14	1.05	1.69	1.35	1.71	2.03	1.53	0.83	1.78	1.91	1.50	1.34	1.28	1.34
Er	3.50	3.44	3.58	3.64	3.32	3.33	3.39	2.97	4.78	3.82	4.57	5.45	4.38	2.31	5.02	5.34	4.47	3.84	3.64	3.68
Tm	0.52	0.51	0.52	0.53	0.46	0.51	0.54	0.44	0.68	0.55	0.67	0.79	0.64	0.34	0.72	0.74	0.68	0.59	0.54	0.58
Yb	3.26	3.25	3.13	3.33	2.83	3.44	3.45	2.87	4.25	3.48	4.31	5.06	4.04	2.21	4.58	4.69	4.46	3.88	3.44	3.77
Lu	0.50	0.49	0.47	0.50	0.41	0.53	0.52	0.45	0.68	0.55	0.68	0.77	0.62	0.35	0.71	0.73	0.67	0.58	0.53	0.54
Hf	9.10	9.17	8.32	8.35	8.36	5.47	7.19	7.29	12.13	10.57	9.18	9.21	9.77	7.20	12.66	14.64	9.37	8.65	8.02	8.31
Ta	1.91	1.19	1.83	1.36	1.23	1.59	1.63	1.22	1.92	1.38	1.78	2.02	1.35	0.63	1.45	2.73	1.59	1.77	2.14	1.52
Pb	25.0	20.2	17.5	20.4	22.2	25.8	20.8	38.4	23.8	104	17.5	23.4	15.7	14.8	17.4	28.3	33.0	30.1	33.8	39.5
Th	25.7	26.1	15.0	20.6	14.0	34.4	30.0	27.7	20.0	13.5	18.7	18.2	21.3	15.3	19.2	22.9	39.0	27.1	25.2	25.7
U	3.39	3.61	2.50	3.29	2.11	5.00	4.81	2.53	2.13	2.10	3.07	3.06	3.18	2.55	2.81	3.06	4.25	4.13	3.96	4.10

The samples with asterisk are enclaves.

Appendix Table 2 (*continued*)

	DA-2-4a	DA-2-5	DA-6-1	DA-6-2	DA-6-3a	DA-6-4	DA-6-5	CF-1	CF-2	CF-3a	CF-3b	CF-3c	CF-4	CF-5	ZX-6-1	ZX-6-2	ZX-6-3	W-2	MRG-1	GSR-1
Major oxides (%)																				
SiO_2	67.12	66.42	63.37	64.80	64.34	62.92	63.30	61.10	62.58	66.68	61.63	60.48	61.73	66.33	67.03	67.68	66.27	52.36	39.17	72.81
TiO_2	0.49	0.50	0.67	0.56	0.58	0.62	0.65	0.75	0.70	0.62	0.78	0.76	0.75	0.48	0.34	0.32	0.34	1.09	3.72	0.29
Al_2O_3	14.17	14.45	16.50	15.86	15.84	15.97	17.12	16.95	16.50	13.85	16.20	17.05	16.23	15.42	15.34	15.36	15.53	14.86	8.22	13.61
FeO	3.66	3.83	4.60	4.25	4.29	4.45	4.11	5.42	5.00	5.48	5.85	5.50	5.38	4.11	3.63	3.59	3.67	10.65	17.70	2.15
MnO	0.07	0.08	0.10	0.09	0.07	0.09	0.10	0.11	0.10	0.12	0.13	0.11	0.08	0.09	0.08	0.08	0.08	0.17	0.17	0.06
MgO	0.83	0.82	1.05	0.74	0.85	0.82	0.53	1.27	1.13	0.41	1.57	1.28	1.19	0.57	0.33	0.30	0.35	6.63	13.49	0.42
CaO	2.21	2.42	3.11	2.35	2.05	2.66	3.42	3.69	3.14	1.85	2.83	2.96	2.25	1.77	1.66	1.86	1.88	10.79	15.03	1.61
Na_2O	2.88	3.02	3.58	3.65	3.56	3.46	3.52	3.07	3.21	3.57	3.08	3.30	3.42	3.70	3.24	3.36	3.17	2.11	0.71	3.28
K_2O	5.59	5.33	5.53	5.87	6.10	6.14	5.75	5.82	6.02	5.39	5.98	6.74	6.03	6.20	6.32	6.26	6.35	0.62	0.18	4.97
P_2O_5	0.16	0.17	0.23	0.16	0.16	0.19	0.20	0.28	0.25	0.18	0.31	0.28	0.29	0.13	0.09	0.08	0.08	0.12	0.05	0.10
LOI	2.87	2.92	1.28	1.68	2.14	2.65	1.30	1.56	1.40	1.91	1.66	1.51	2.66	1.22	1.91	1.15	2.31	0.60	1.56	0.69
Total	100.05	99.96	100.01	100.02	100.00	99.97	100.01	100.02	100.02	100.08	100.01	99.98	100.01	100.03	99.99	100.02	100.04	100.01	99.99	100.00
ACNK	0.96	0.95	0.94	0.95	0.98	0.93	0.94	0.94	0.94	0.92	0.97	0.94	1.00	0.96	1.01	0.98	1.00			
Trace elements (ppm)																				
V	31.3	33.7	33.1	32.4	28.4	30.3	28.1	45.3	40.7	39.7	48.5	49.2	55.9	19.0	15.4	12.0	15.3	261	525	24.6
Cr	4.63	5.54	9.58	6.55	5.48	6.10	6.96	8.86	6.80	8.44	12.99	9.26	8.20	8.19	6.8	10.5	7.42	87.9	436	11.2
Co	4.51	4.63	6.59	4.36	4.56	4.58	4.35	7.62	6.92	6.54	8.62	7.02	7.49	3.11	2.65	1.99	2.56	43.6	86.0	2.79
Ni	10.9	6.83	5.14	2.04	2.31	8.47	4.71	3.71	3.25	3.43	7.74	4.29	3.42	3.96	2.21	1.76	1.73	85.7	200	5.45
Ga	18.4	19.3	19.8	20.7	20.4	19.9	19.4	20.1	19.7	19.3	19.7	19.3	20.0	20.0	20.4	20.6	20.0	17.6	17.9	20.2
Ge	1.54	1.29	1.17	1.42	1.18	1.51	1.38	1.01	1.04	1.15	1.06	1.05	1.14	1.33	1.52	1.29	1.34	1.83	1.49	2.31
Rb	254	218	151	173	179	167	134	150	154	141	147	158	158	181	185	175	186	19.0	7.34	466
Sr	187	168	452	428	306	317	421	454	403	363	433	421	399	170	173	227	151	187	253	111
Y	33.5	37.1	26.0	27.6	27.4	28.0	22.9	25.4	27.5	25.3	27.1	25.8	25.7	29.9	24.4	22.5	23.2	20.6	12.9	62.9
Zr	312	296	393	417	408	496	380	307	286	309	299	279	279	478	524	333	546	102	105	152
Nb	20.4	18.2	18.0	19.1	19.1	16.2	14.1	13.8	14.9	14.7	14.3	14.9	14.5	18.4	14.1	14.1	14.7	7.82	18.6	32.0
Cs	6.09	6.58	4.35	4.15	4.94	4.30	2.94	2.78	2.73	2.29	2.45	2.32	4.96	2.61	3.03	4.42	2.81	0.91	0.68	38.4
Ba	786	672	1460	1037	954	1014	1570	1364	1513	1267	1481	1440	1343	641	1336	1151	1379	168	55.8	334
La	62.2	60.3	92.1	138	138	125	66.7	83.7	85.9	82.8	85.8	82.8	87.4	159	216	173	187	10.3	8.67	55.8
Ce	121	116	173	256	254	219	120	149	164	147	164	147	162	275	368	296	323	23.9	23.9	111
Pr	14.4	14.0	18.4	26.5	26.4	24.3	14.0	17.0	17.6	16.8	17.6	16.9	17.6	28.4	39.4	29.7	34.9	3.03	3.73	13.5
Nd	53.0	52.7	64.9	89.2	89.3	86.0	51.0	61.7	62.2	59.5	63.2	60.4	62.5	95.6	130.4	98.2	115	13.2	18.0	49.4
Sm	9.83	9.82	9.57	11.9	11.8	11.5	8.06	9.27	9.57	9.05	9.66	9.15	9.53	12.5	14.5	12.0	13.5	3.13	4.25	10.1
Eu	1.44	1.32	2.29	1.76	1.70	1.75	2.31	2.60	2.36	2.26	2.33	2.32	2.49	1.53	1.73	1.67	1.90	1.03	1.32	0.87
Gd	7.90	8.37	7.69	8.89	8.95	7.07	5.68	7.71	7.87	7.34	7.94	7.48	7.72	9.59	8.78	8.34	8.16	3.66	4.01	9.38
Tb	1.29	1.31	0.96	1.07	1.07	1.16	0.85	0.97	1.01	0.95	1.02	0.99	1.01	1.14	1.04	0.87	0.97	0.59	0.56	1.71
Dy	6.88	7.47	5.06	5.42	5.54	6.00	4.61	4.86	5.10	4.94	5.29	5.00	5.02	5.88	5.25	4.46	4.97	3.63	2.81	10.4
Ho	1.28	1.41	0.97	1.01	1.03	1.10	0.86	0.94	1.01	0.96	0.99	0.95	0.96	1.13	0.95	0.83	0.88	0.72	0.49	2.09
Er	3.55	3.91	2.71	2.81	2.86	3.16	2.43	2.49	2.73	2.59	2.68	2.65	2.56	3.08	2.75	2.23	2.71	2.02	1.10	6.52
Tm	0.53	0.61	0.38	0.41	0.42	0.47	0.36	0.36	0.40	0.37	0.39	0.36	0.37	0.46	0.41	0.34	0.39	0.31	0.16	1.07
Yb	3.49	4.05	2.56	2.74	2.76	3.04	2.40	2.34	2.61	2.42	2.46	2.43	2.34	3.08	2.58	2.22	2.47	1.89	0.90	7.47
Lu	0.53	0.59	0.41	0.43	0.44	0.47	0.37	0.37	0.40	0.38	0.39	0.37	0.37	0.47	0.42	0.35	0.39	0.29	0.12	1.16
Hf	9.11	8.92	8.00	8.49	8.36	12.5	9.34	6.60	6.52	6.81	6.54	6.19	6.27	9.61	12.6	7.66	12.5	2.65	3.80	5.87
Ta	1.33	1.73	1.07	1.07	1.10	1.22	1.54	0.83	0.92	0.89	0.87	0.89	0.90	1.13	1.15	0.82	1.17	0.60	0.69	7.62
Pb	30.2	35.2	22.8	25.9	25.5	43.3	33.2	22.8	23.3	26.5	23.6	23.8	23.6	28.4	36.2	41.5	26.1	10.397	3.35	28.0
Th	24.4	26.5	19.2	25.0	24.0	23.3	14.8	17.0	19.5	18.1	18.0	17.7	18.9	28.8	28.3	25.2	25.7	2.15	0.79	54.0
U	3.66	4.45	2.87	3.03	3.08	3.16	2.23	2.60	2.51	3.05	2.89	2.76	2.79	3.35	2.58	3.17	3.14	0.56	0.24	18.8

Appendix Table 3
Sr and Nd isotopic data of shoshonitic rocks from the northern Wuyi Mountains.

Sample	$^{87}Rb/^{86}Sr$	$^{87}Sr/^{86}Sr$	±2σ	I_{Sr}	$^{147}Sm/^{144}Nd$	$^{143}Nd/^{144}Nd$	±2σ	T_{DM} (Ga)	εNd(t)
Y-1-1	2.36	0.713225	0.000016	0.70873	0.098	0.512055	0.000009	1.44	−9.68
Y-1-4	1.13	0.711124	0.000013	0.70897	0.100	0.512073	0.000009	1.44	−9.37
Y-1-5	0.69	0.710424	0.000016	0.70911	0.099	0.512070	0.000011	1.43	−9.41
Y-1-6	5.86	0.719930	0.000016	0.70876	0.102	0.512071	0.000010	1.47	−9.45
Y-3a	4.52	0.716918	0.000013	0.70831	0.101	0.512038	0.000008	1.50	−10.06
D-1	9.99	0.728803	0.000013	0.70906	0.094	0.512173	0.000009	1.24	−7.24
D-2-1	4.49	0.716753	0.000019	0.70789	0.113	0.512197	0.000010	1.44	−7.12
D-2-3	3.37	0.714370	0.000016	0.70772	0.110	0.512217	0.000010	1.37	−6.69
D-6-2	1.21	0.710579	0.000016	0.70820	0.082	0.512178	0.000008	1.12	−6.94
D-6-3a	1.75	0.711591	0.000019	0.70814	0.081	0.512155	0.000009	1.15	−7.38
D-6-4	1.52	0.711014	0.000013	0.70801	0.081	0.512088	0.000011	1.22	−8.67
D-6-5	0.92	0.709672	0.000013	0.70785	0.095	0.512186	0.000010	1.24	−7.02
Z-6-1	3.10	0.717232	0.000019	0.71119	0.067	0.511983	0.000011	1.22	−10.52
Z-6-2	2.26	0.715758	0.000010	0.71136	0.073	0.512028	0.000011	1.21	−9.74
Z-6-3	3.56	0.718502	0.000019	0.71156	0.071	0.512000	0.000012	1.23	−10.26
H-4	3.72	0.715547	0.000013	0.70889	0.106	0.512152	0.000011	1.41	−8.03
H-6	3.30	0.714560	0.000026	0.70865	0.105	0.512266	0.000009	1.24	−5.79
H-7	5.72	0.719959	0.000019	0.70972	0.109	0.512261	0.000010	1.29	−5.94
H-9	1.16	0.718272	0.000013	0.71619	0.093	0.512263	0.000008	1.12	−5.65
H-10a	11.9	0.734770	0.000019	0.71343	0.104	0.512273	0.000009	1.22	−5.63
C-1	1.01	0.711001	0.000016	0.70923	0.092	0.512124	0.000009	1.28	−8.39
C-2	1.18	0.711161	0.000014	0.70910	0.093	0.512150	0.000010	1.26	−7.89
C-3a	5.04	0.719500	0.000013	0.71069	0.108	0.512146	0.000012	1.45	−8.21
C-3c	1.19	0.711287	0.000020	0.70921	0.092	0.512077	0.000010	1.35	−9.31
C-5	3.18	0.715545	0.000014	0.70999	0.080	0.512129	0.000008	1.16	−8.10

Appendix Table 4
Zircon Hf isotopic data of shoshonitic rocks from the northern Wuyi Mountains.

Spot #	$^{176}Lu/^{177}Hf$	$^{176}Hf/^{177}Hf$	±2σ	εHf(t)	±2σ	TDM (Ga)	TDM^{C}(Ga)
Z6-2, age = 137 Ma							
1	0.00085	0.282452	0.000025	−8.4	0.4	1.13	1.72
2	0.00148	0.282366	0.000028	−11.5	0.5	1.27	1.92
3	0.00181	0.282421	0.000027	−9.6	0.5	1.20	1.80
4	0.00113	0.282405	0.000024	−10.1	0.4	1.20	1.83
5	0.00068	0.282390	0.000028	−10.6	0.5	1.21	1.86
6	0.00033	0.282393	0.000022	−10.4	0.4	1.19	1.85
7	0.00101	0.282401	0.000030	−10.2	0.5	1.20	1.84
8	0.00196	0.282417	0.000022	−9.7	0.4	1.21	1.81
9	0.00087	0.282414	0.000023	−9.7	0.4	1.18	1.81
10	0.00104	0.282400	0.000023	−10.2	0.4	1.20	1.84
11	0.00114	0.282374	0.000024	−11.2	0.4	1.25	1.90
Y1-1 01, age = 134 Ma							
1	0.00096	0.282450	0.000026	−8.5	0.5	1.13	1.73
2	0.00128	0.282466	0.000029	−8.0	0.5	1.12	1.70
3	0.00125	0.282512	0.000029	−6.4	0.5	1.05	1.60
4	0.00121	0.282441	0.000025	−8.9	0.4	1.15	1.75
5	0.00076	0.282461	0.000025	−8.1	0.4	1.11	1.71
6	0.00115	0.282473	0.000028	−7.7	0.5	1.11	1.68
7	0.00155	0.282451	0.000023	−8.6	0.4	1.15	1.73
8	0.00215	0.282472	0.000041	−7.9	0.7	1.14	1.69
9	0.00083	0.282465	0.000027	−8.0	0.5	1.11	1.70
10	0.00103	0.282425	0.000035	−9.4	0.6	1.17	1.79
11	0.00065	0.282401	0.000033	−10.3	0.6	1.19	1.84
12	0.00147	0.282400	0.000057	−10.3	1.0	1.22	1.85
13	0.00098	0.282469	0.000035	−7.9	0.6	1.11	1.69
14	0.00125	0.282430	0.000034	−9.3	0.6	1.17	1.78
15	0.00085	0.282407	0.000031	−10.1	0.5	1.19	1.83
D2-3, age = 139 Ma							
1	0.00088	0.282464	0.000026	−7.9	0.5	1.11	1.70
2	0.00100	0.282474	0.000025	−7.6	0.4	1.10	1.67
3	0.00074	0.282466	0.000018	−7.8	0.3	1.10	1.69
4	0.00138	0.282489	0.000034	−7.1	0.6	1.09	1.64
5	0.00142	0.282320	0.000037	−13.1	0.7	1.33	2.02
6	0.00085	0.282497	0.000025	−6.8	0.4	1.06	1.62
7	0.00138	0.282471	0.000032	−7.7	0.6	1.12	1.68
8	0.00093	0.282424	0.000023	−9.3	0.4	1.17	1.79
9	0.00089	0.282473	0.000029	−7.6	0.5	1.10	1.68
10	0.00072	0.282361	0.000040	−11.5	0.7	1.25	1.93
11	0.00283	0.282589	0.000085	−3.7	1.5	0.99	1.43

Appendix Table 4 (*continued*)

Spot #	$^{176}Lu/^{177}Hf$	$^{176}Hf/^{177}Hf$	±2σ	εHf(t)	±2σ	TDM (Ga)	TDM^{C}(Ga)
Hong-4, age = 125 Ma							
01	0.00258	0.282407	0.000063	−10.4	1.1	1.25	1.84
02	0.00178	0.282562	0.000028	−4.8	0.5	1.00	1.49
03	0.00279	0.282699	0.000056	−0.1	1.0	0.82	1.19
04	0.00100	0.282481	0.000025	−7.6	0.4	1.09	1.67
05	0.00186	0.282648	0.000028	−1.8	0.5	0.88	1.30
06	0.00101	0.282646	0.000033	−1.8	0.6	0.86	1.30
07	0.00209	0.282548	0.000039	−5.4	0.7	1.03	1.52
08	0.00185	0.282584	0.000034	−4.1	0.6	0.97	1.44
09	0.00156	0.282499	0.000038	−7.1	0.7	1.08	1.63
10	0.00177	0.282763	0.000081	2.3	1.4	0.71	1.04
11	0.00194	0.282539	0.000042	−5.7	0.7	1.03	1.54
12	0.00139	0.282547	0.000025	−5.3	0.4	1.01	1.52
13	0.00081	0.282523	0.000023	−6.1	0.4	1.03	1.57
14	0.00062	0.282513	0.000033	−6.5	0.6	1.03	1.59
15	0.00082	0.282582	0.000021	−4.0	0.4	0.94	1.44
16	0.00110	0.282579	0.000026	−4.2	0.5	0.95	1.45
17	0.00075	0.282425	0.000025	−9.6	0.4	1.16	1.79
18	0.00067	0.282579	0.000028	−4.1	0.5	0.94	1.45
19	0.00185	0.282514	0.000024	−6.5	0.4	1.07	1.60
20	0.00116	0.282599	0.000031	−3.5	0.5	0.93	1.40
21	0.00083	0.282648	0.000052	−1.7	0.9	0.85	1.29

Calculated processes and parameters are similar as Li et al. (2007).

References

Bao, Z.W., Zhao, Z.H., Xiong, X.L., 2000. Geochemistry of Ejinao alkali syenite and its geodynamic significance. Geochimica 29 (5), 462–468.

Black, L.P., Kamo, S.L., Allen, C.M., Aleinikoff, J.N., Davis, D.W., Korsch, R.J., Foudoulis, C., 2003. TEMORA 1: a new zircon standard for Phanerozoic U–Pb geochronology. Chemical Geology 200, 155–170.

Campbell, I.H., Stepanov, A.S., Liang, H.Y., Allen, C.M., Norman, M.C., Zhang, Y.Q., Xie, Y.W., 2014. The origin of shoshonites: new insights from the Tertiary high-potassic intrusions of eastern Tibet. Lithos 167, 983.

Cen, T., Li, W.X., Wang, X.C., Pang, C.J., Li, Z.X., Xing, G.F., Zhao, X.L., Tao, J.H., 2016. Petrogenesis of early Jurassic basalts in southern Jiangxi Province, South China: implications for the thermal state of the Mesozoic mantle beneath South China. Lithos 256–257, 311–330.

Chen, J.F., Zhou, T.X., Yin, C.S., 1991. ^{40}Ar–^{39}Ar dating of several Mesozoic plutons in southeastern Zhejiang province. Acta Petrologica Sinica 3, 37–44.

Chen, C.H., Lee, C.Y., Shinjo, R., 2008. Was there Jurassic paleo-Pacific subduction in South China?: constraints from $^{40}Ar/^{39}Ar$. Lithos 106, 83–92.

Chung, S.L., Lo, C.H., Lee, T.Y., Zhang, Y.Q., Xie, Y.W., Li, X.H., Wang, K.L., Wang, P.L., 1998. Diachronous uplift of the Tibet Plateau starting 40 Myr ago. Nature 394, 769–773.

Conceicao, R.V., Green, D.H., 2004. Derivation of potassic (shoshonitic) magmas by decompression melting of phlogopite + pargasite lherzolite. Lithos 72, 209–224.

Conticelli, S., Peccerillo, A., 1992. Petrology and geochemistry of potassic and ultrapotassic volcanism in central Italy: petrogenesis and inferences on the evolution of the mantle source. Lithos 28, 221–240.

Cumming, G.L., Richards, J.R., 1975. Ore lead isotope ratios in a continuously changing Earth. Earth and Planetary Science Letters 28, 155–171.

Defant, M.J., Drummond, M.S., 1993. Mount St. Helens: potential example of the partial melting of the subducted lithosohere in a volcanic arc. Geology 21, 547–550.

Duggen, S., Hoernle, K., van den Bogaard, P., Rüpke, L., Morgan, J.P., 2003. Deep roots of the Messinian salinity crisis. Nature 422, 602–606.

Duggen, S., Hoernle, K., van den Bogaard, P., Garbe-SchÖnberg, D., 2005. Post-collisional transition from subduction- to intraplate-type magmatism in the westernmost Mediterranean: evidence for continental-edge delamination of subcontinental lithosphere. Journal of Petrology 46, 1155–1201.

Elkins-Tanton, L.T., Grove, T.L., 2003. Evidence for deep melting of hydrous metasomatized mantle: Pliocene high-potassium magmas from the Sierra Nevadas. Journal of Geophysical Research 108 (B7):2350. http://dx.doi.org/10.1029/2002JB002168.

English, J.M., Johnston, S.T., Wang, K., 2003. Thermal modeling of the Laramide orogeny: testing the flat-slab subduction hypothesis. Earth and Planetary Science Letters 214, 619–632.

Erdman, M.E., Lee, C.T.A., Levander, A., Jiang, H., 2016. Role of arc magmatism and lower crustal foundering in controlling elevation history of the Nevadaplano and Colorado Plateau: a case study of pyroxenitic lower crust from central Arizona, USA. Earth and Planetary Science Letters 439, 48–57.

Feeley, T.C., 2003. Origin and tectonic implications of across-strike geochemical variations in the Eocene Absaroka volcanic province, United States. The Journal of Geology 111, 329–346.

Feeley, T.C., Cosca, M.A., 2003. Time v. composition trends of magmatism at Sunlinght volcano, Absaroka volcanic province, Wyoming. Geological Society of America Bulletin 115, 714–728.

Foley, S., 1992. Vein-plus-wall-rock melting mechanisms in the lithosphere and the origin of potassic alkaline magmas. Lithos 28, 435–453.

Griffin, W.L., Pearson, N.J., Belousova, E.A., Saeed, A., 2006. Common: Hf-isotope heterogeneity in standard zircon 91500. Chemical Geology 233, 358–363.

Gualda, G.A.R., Ghiorso, M.S., Lemons, R.V., Carley, T.L., 2012. Rhyolite-MELTS: a modified calibration of MELTS optimized for silica-rich, fluid-bearing magmatic systems. Journal of Petrology 53, 875–890.

Gutscher, M.A., Maury, R., Eissen, J.P., Bourdon, E., 2000. Can slab melting be caused by flat subduction. Geology 28, 535–538.

He, Z.Y., Xu, X.S., 2012. Petrogenesis of the Late Yanshanian mantle-derived intrusions in southeastern China: response to the geodynamics of paleo-Pacific plate subduction. Chemical Geology 328, 208–221.

He, Z.Y., Xu, X.S., Wang, X.L., Chen, R., 2008. Geochronology and geochemistry of shoshonitic volcanics in southern Jiangxi province. Acta Petrologica Sinica 24 (11), 2524–2536.

Jahn, B.M., Chen, P.Y., Yen, T.P., 1976. Rb–Sr ages of granitic rocks in southeastern China and their tectonic significance. Geological Society of America Bulletin 86, 763–776.

Janoušek, V., Finger, F., Roberts, M., Frýda, J., Pin, C., Dolejš, D., 2004. Deciphering the petrogenesis of deeply buried granites: whole-rock geochemical constraints on the origin of largely undepleted granulites from the Moldanubian Zone of the Bohemian Massif. Transactions of the Royal Society of Edinburgh: Earth Sciences 95, 141–159.

Kay, R.W., Kay, S.M., 1993. Delamination and delamination magmatism. Tectonophysics 219, 177–189.

Lan, C.Y., Jahn, B.M., Mertzman, S.A., Wu, T.W., 1996. Subduction-related granitic rock of Taiwan. Journal of Southeast Asian Earth Sciences 14, 11–28.

Lapierre, H., Jahn, B.M., Charvet, J., Yu, Y.W., 1997. Mesozoic magmatism in Zhejiang Province and its relation with the tectonic activities in SE China. Tectonophysics 274, 321–338.

Lee, C.T.A., 2005. Trace-element evidence for hydrous metasomatism at the base of the North American lithosphere and possible association with Laramide low angle subduction. Journal of Geology 113, 673–685.

Li, X.H., 1997. Timing of the Cathaysia block formation: constraints from SHRIMP U–Pb zircon geochronology. Episodes 20, 188–192.

Li, X.H., 2000. Cretaceous magmatism and lithosphere extension in Southeast China. Journal of Asian Earth Science 18, 293–305.

Li, Z.X., Li, X.H., 2007. Formation of the 1300-km-wide intracontinental orogen and postorogenic magmatic province in Mesozoic South China: a flat-slab subduction modal. Geology 35 (2), 179–182.

Li, W.X., Zhou, X.M., 2000. Origin of late Mesozoic igneous rocks in coastal region of Zhejiang and Fujian provinces: constraint in geochemistry. Progress in Natural Science 10 (7), 630–640 (in Chinese).

Li, X.H., Liu, Y., Tu, X.L., Hu, G.Q., Zeng, W., 2002. Precise determination of chemical compositions in silicate rocks using ICP-AES and ICP-MS: a comparative study of sample digestion techniques of alkali fusion and acid dissolution. Geochimica 31, 289–294 (in Chinese with English abstract).

Li, X.H., Chen, Z.G., Liu, D.Y., Li, W.X., 2003. Jurassic gabbro-geanite-syenite suites from Southern Jiangxi province, SE China: age, origin, and tectonic significance. International Geology Review 45, 898–921.

Li, X.H., Chung, S.L., Zhou, H.W., Lo, C.H., Liu, Y., Chen, C.H., 2004a. Jurassic intraplate magmatism in southeastern Hunan-eastern Guangxi: $^{40}Ar/^{39}Ar$ dating, geochemistry, Sr–Nd isotopes and implications for the tectonic evolution of SE China. In: Malpas, J., Fletcher, C.J.N., Ali, J.R., Aitchison, J.C. (Eds.), Aspects of the Tectonic Evolution of China. Geologcial Society, London, Special Publications Vol. 226, pp. 193–215.

Li, X.H., Liu, D.Y., Sun, M., Li, W.X., Liang, X.R., Liu, Y., 2004b. Precise Sm–Nd and U–Pb isotopic dating of the super-giant Shizhuyuan polymetallic deposit and its host granite, Southeast China. Geological Magazine 141, 225–231.

Li, W.X., Li, X.H., Li, Z.X., 2005. Neoproterozoic bimodal magmatism in the Cathaysia Block of South China and its tectonic significance. Precambrian Research 136, 51–66.

Li, X.H., Li, Z.X., Li, W.X., Wang, Y.J., 2006. Initiation of the Indosinian Orogeny in South China: evidence for a Permian Magmatic Arc on Hainan Island. Journal of Geology 114, 341–353.

Li, X.H., Li, Z.X., Li, W.X., Liu, Y., Yuan, C., Wei, J., Qi, C.S., 2007. U–Pb zircon, geochemical and Sr–Nd–Hf isotopic constraints on age and origin of Jurassic I- and A-type granites from central Guangdong, SE China: a major igneous event in response to foundering of a subducted flat-slab? Lithos 96, 186–204.

Li, W.X., Li, X.H., Li, Z.X., Lou, F.S., 2008. Obduction-type granites within the NE Jiangxi Ophiolite: implications for the final amalgamation between the Yangtze and Cathaysia Blocks. Gondwana Research 13:288–301. http://dx.doi.org/10.1016/j.gr.2007.12.010.

Li, X.H., Li, W.X., Li, Z.X., Lo, C.H., Wang, J., Ye, M.F., Yang, Y.H., 2009. Amalgamation between the Yangtze and Cathaysia Blocks in South China: constraints from SHRIMP U–Pb zircon ages, geochemistry and Nd-Hf isotopes of the Shuangxiwu volcanic rocks. Precambrian Research 174:117–128. http://dx.doi.org/10.1016/j.precamres.2009.07.004.

Li, Z.X., Li, X.H., Wartho, J.A., Clark, C., Li, W.X., Zhang, C.L., Bao, C.M., 2010. Magmatic and metamorphic events during the early Paleozoic Wuyi–Yunkai orogeny, southeastern South China: new age constraints and pressure-temperature conditions. Geological Society of America Bulletin 122 (5/6):771–793. http://dx.doi.org/10.1130/B30021.1.

Li, X.H., Li, Z.X., He, B., Li, W.X., Li, Q.L., Gao, Y., Wang, X.C., 2012a. The Early Permian active continental margin and crustal growth of the Cathaysia Block: in situ U–Pb, Lu–Hf and O isotope analyses of detrital zircons. Chemical Geology 328, 195–207.

Li, Z.X., Li, X.H., Chung, S.L., Lo, Q.H., Xu, X.S., Li, W.X., 2012b. Magmatic switch-on and switch-off along the South China continental margin since the Permian: transition from an Andean-type to a Western Pacific-type plate boundary. Tectonophysics 532-535, 271–290.

Li, J.H., Zhang, Y.Q., Dong, S.W., Johnston, S.T., 2014a. Cretaceous tectonic evolution of South China: a preliminary synthesis. Earth-Science Reviews 134, 98–136.

Li, Z., Qiu, J.S., Yang, X.M., 2014b. A review of the geochronology and geochemistry of Late Yanshanian (Cretaceous) pluton along the Fujian coastal area of southeastern China: implications for magma evolution related to slab break-off and rollback in the Cretaceous. Earth-Science Reviews 128, 232–248.

Li, L., Xu, X.S., Xia, Y., 2014c. Cretaceous Pacific plate movement beneath SE China: evidence from episodic volcanism and related intrusions. Tectonophysics 614, 170–184.

Lloyd, F.E., Arima, M., Edgar, A.D., 1985. Partial melting of a phlogopite-clinopyroxenite nodule from south-west Uganda: an experimental study bearing on the origin of highly potassic continental rift volcanics. Contributions to Mineralogy and Petrology 91, 321–329.

Lu, C.Z., Yan, T.Z., Dong, C.W., Gu, M.G., 2006a. Magmatic consanguinity analysis of the Muchen intrusion and Xishantou Formation volcanic rocks in Zhejiang. Geology in China 33 (1), 146–152.

Lu, C.Z., Wang, Q.H., Dong, C.W., Dong, X.F., 2006b. Geochemical characteristics of the Honggong aluminous A-type granite pluton in Zhejiang province and its tectonic setting. Geological Journal of China Universities 12 (4), 500–506.

Manley, C.R., Glazner, A.F., Farmer, G.L., 2000. Timing of volcanism in the Sierr Nevada of California: evidence for Pliocene delamination of the batholithic root? Geology 28, 811–814.

Martin, H., Bonin, B., Capdevila, R., Jahn, B.M., Lameyre, J., Wang, Y., 1994. The Kuiqi peralkaline granitic complex (SE China): petrology and geochemistry. Journal of Petrology 35, 983–1015.

Meng, L.F., Li, Z.X., Chen, H.L., Li, X.H., Wang, X.C., 2012. Geochronological and geochemical results from Mesozoic basalts in southern South China Block support the flat-slab subduction model. Lithos 132-133, 127–140.

Middlemost, E.A.K., 1994. Naming materials in the magma/igneous rock system. Earth Science Reviews 37, 215–224.

Mitchell, R.H., 1995. Melting experiments on a sanidine phlogopite lamproite at 4–7 GPa and their bearing on the source of lamproite magma. Journal of Petrology 36, 1455–1475.

Peccerillo, A., Taylor, S.R., 1976. Geochemistry of Eocene calc-alkaline volcanic rocks from the Kastamonu area, northern Turkey. Contributions to Mineralogy and Petrology 58, 130–143.

Peccerillo, A., Barberio, M.R., Yirgu, G., Ayalew, D., Barbieri, M., Wu, T.W., 2003. Relationship between mafic and peralkaline felsic magmatism in continental rift settings: a petrological, geochemical and isotopic study of the Gedemsa Volcano, Central Ethiopian Rift. Journal of Petrology 44, 2003–2032.

Pe-piper, G., Piper, D.J.W., Koukouvelas, I., Dolansky, L.M., Kokkalas, S., 2009. Postorogenic shoshonitic rocks and their origin by melting underplated basalts: the Miocene of Limnos, Greece. Geological Society of America Bulletin 121, 39–54.

Roberts, M.P., Clemens, J.D., 1993. Origin of high-potassium, calc-alkaline, I-type granitoids. Geology 21, 825–828.

Rudnick, R.L., Fountain, D.M., 1995. Nature and composition of the continental crust: a lower crustal perspective. Reviews of Geophysics 33, 267–309.

Saleeby, J., 2003. Segmentation of the Laramide Slab—evidence from the southern Sierra Nevada region. Geological Society of America Bulletin 115, 655–668.

Sewell, R.J., Campbell, S.D.G., 1997. Geochemistry of coeval Mesozoic plutonic and volcanic suites in Hong Kong. Journal of the Geological Society, London 154, 1053–1066.

Sisson, T.W., Ratajeski, K., Hankins, W.B., 2005. Voluminous granitic magmas from common basaltic source. Contributions to Mineralogy and Petrology 148, 635–661.

Smith, D., 2013. Olivine thermometry and source constraints for mantle fragments in the Navajo Volcanic Field, Colorado Plateau, southwest United States: implications for the mantle wedge. Geochemistry, Geophysics, Geosystems 14, 693–711.

Sommer, H., Gauert, C., 2011. Hydrating laterally extensive regions of continental lithosphere by flat subduction: a pilot study from the North American Cordillera. Journal of Geodynamics 51, 17–24.

Tanaka, T., et al., 2000. JNdi-1: a neodymium isotopic reference in consistency with LaJolla neodymium. Chemical Geology 168, 279–281.

Turner, S., Hawkerworth, C., Liu, J., Rogers, N., Kelley, S., van Calsteren, P., 1993. Timing of Tibetan uplift constrained by analysis of volcanic rocks. Nature 364, 50–53.

Turner, S., Arnaud, N., Liu, J., Rogers, N., Hawkesworth, C., Harris, N., Kelley, S., Calsteren, P.V., Deng, W., 1996. Post-collision, shoshonitic volcanism on the Tibetan Plateau: implications for convective thinning of the lithosphere and the source of ocean island basalts. Journal of Petrology 37, 45–71.

Vielzeuf, D., Holloway, J.R., 1988. Experimental determination of the fluid-absent melting reactions in the politic system. Contributions to Mineralogy and Petrology 98, 257–267.

Wang, J., Li, Z.X., 2003. History of Neoproterozoic rift basins in South China: implications for Rodinia break-up. Precambrian Research 122, 141–158.

Wang, Q., Li, J.W., Jian, P., Zhao, Z.H., Xiong, X.L., Bao, Z.W., Xu, J.F., Li, C.F., Ma, J.L., 2005. Alkaline syenites in eastern Cathaysia (South China): link to Permian-Triassic transtension. Earth and Planetary Science Letters 230, 339–354.

Wei, G.J., Liang, X.R., Li, X.H., Liu, Y., 2002. Precise measurement of Sr isotopic compositions of liquid and solid base using (LP) MCICP- MS. Geochimica 31, 295–305 (in Chinese with English abstract).

White, A.J.R., Chappell, B.M., 1983. Granitoids types and their distribution in the Lachlan Fold Belt, southeastern Australia. Geological Society of America Memoirs 159, 21–34.

Williams, I.S., 1998. U–Th–Pb geochronology by ion microprobe. Applications of microanalytical techniques to understanding mineralizing processes. Reviews in Economic Geology 7, 1–35.

Williams, H.M., Turner, S.P., Pearce, J.A., Kelley, S.P., Harris, N.B.W., 2004. Nature of the source regions for post-collisional, potassic magmatism in southern and northern Tibet from geochemical variations and inverse trace element modelling. Journal of Petrology 45, 555–607.

Wu, F.Y., Yang, Y.H., Xie, L.W., Yang, J.H., Xu, P., 2006. Hf isotopic compositions of the standard zircons and baddeleyites used in U–Pb geochronology. Chemical Geology 234, 105–126.

Yao, W.H., Li, Z.X., Li, W.X., Wang, X.C., Li, X.H., Yang, J.H., 2012. Post-kinematic lithospheric delamination of the Wuyi–Yunkai orogen in South China: evidence from ca. 435 Ma high-Mg basalts. Lithos 154, 115–129.

Ye, M.F., Li, X.H., Li, W.X., Liu, Y., Li, Z.X., 2007. SHRIMP zircon U–Pb geochronological and whole-rock geochemical evidence for an early Neoproterozoic Sibaoan magmatic arc along the southeastern margin of the Yangtze Block. Gondwana Research 12: 144–156. http://dx.doi.org/10.1016/j.gr.2006.09.001.

Yu, J.H., Wang, L., O'Reilly, S.Y., Griffin, W.L., Zhang, M., Li, C., Shu, L., 2009. A Paleproterozoic orogeny recorded in a long-lived cratonic remnant (Wuyishan terrane), eastern Cathaysia Block, China. Precambrian Research 174, 347–363.

Zhou, X.M., Li, W.X., 2000. Origin of Late Mesozoic igneous rocks in Southeastern China: implications for lithosphere subduction and underplating of mafic magmas. Tectonophysics 326, 269–287.

Zhou, X.M., Sun, T., Shen, W.X., Shu, L.S., Niu, Y.L., 2006. Petrogenesis of Mesozoic granitoids and volcanic rocks in South China: a response to tectonic evolution. Episodes 29, 26–33.

Zhu, J.C., Xie, C.F., Zhang, P.H., Yang, C., Gu, C.Y., 2005. Niumiao and Tong'an intrusive bodies of NE Guangxi: petrology, zircon SHRIMP U–Pb geochronology and geochemistry. Acta Petrologica Sinica 21 (3), 665–676 (in Chinese with English abstract).

Zhu, J.C., Zhang, P.H., Xie, C.F., Zhang, H., Yang, C., 2006. Magma mixing origin of the mafic enclaves in Lisong granite, NE Guangxi western Nanling Mountains. Geochimica 35 (5), 506–516 (in Chinese with English Abstract).